

This manuscript has undergone peer-review and has been accepted for publication in the journal Basin Research but has not undergone typesetting by the publisher. The final version is available at the following address: <https://doi.org/10.1111/bre.12608>

1 Reflection Seismic Thermometry

2 **Arka Dyuti Sarkar^{1,2}**

3 **Mads Huuse¹**

4 ²Corresponding author: arkadyuti.sarkar@manchester.ac.uk

5 ¹Basins Research Group, Department of Earth and Environmental Sciences, University of
6 Manchester, Manchester M13 9PL, United Kingdom

7 Abstract

8 The North Viking Graben (NVG) is part of the mature North Sea Basin petroleum province and
9 designated as a major carbon storage basin for NW Europe. It has been extensively drilled
10 over five decades with an abundance of well and seismic data in the public domain. As such
11 it serves as an excellent setting to demonstrate the efficacy of a reflection seismic data led
12 approach to predicting subsurface temperatures using a state-of-the-art full waveform
13 inversion velocity model covering the entire NVG. In a forward modelling approach, an
14 empirical velocity to thermal conductivity transform is used in conjunction with predefined
15 heatflow to predict subsurface temperature. The predefined heatflow parameters are set
16 based on the range of values from previous studies in the area. Abundant well data with
17 bottom hole temperature (BHT) records provide calibration of results. In the second step of
18 inverse modelling, BHT's as well as the velocity derived thermal conductivity are used to
19 evaluate a 1D steady state approximation of Fourier's Law for heatflow. In this way heatflow
20 is estimated over the 12000 km² model area at a km scale (lateral) resolution, highlighting
21 lateral variability in comparison to the traditional point-based heatflow datasets. This
22 heatflow is used to condition a final iterative loop of forward modelling to produce a

23 temperature model that is best representative of the subsurface temperature. Calibration
24 against 139 exploration wells indicate that the predicted temperatures are on average only
25 0.6 °C warmer than the recorded values, with a root mean squared error of 5 °C. BHT for the
26 recently completed Northern Lights carbon capture and sequestration (CCS) well 31/5-7 (Eos)
27 has been modelled to be 97 °C, which is 6 °C below the recorded BHT. This highlights the
28 applicability of this workflow not only towards enhancing petroleum systems modelling work
29 but also for use in the energy transition and for fundamental scientific purposes.

30 Highlights

- 31 • Estimating subsurface temperature using seismic reflection and velocity data
- 32 • Empirical velocity thermal conductivity transform
- 33 • Tested in the mature northern North Sea, calibrating results against bottom hole
34 temperatures (BHT) from 139 wells
- 35 • Inverse modelling allows derivation of laterally varying heat flow at resolution of tens
36 of km scale
- 37 • Blind tested workflow to estimate BHT from Northern Lights CCS exploration borehole
38 31/5-7 to within 6 °C of reported BHT

39 **Keywords:**

40 *Seismic; velocity modelling; subsurface temperature; heatflow*

41 **Acknowledgement**

42 This project was enabled by generous funding from Arka's parents, to whom the authors are
43 very grateful. Thanks go to CGG for provision of the North Viking Graben dataset and to
44 Schlumberger for provision of Petrel licenses (the software used for modelling). The authors
45 would like to thank Daniel Schmid, Christian Hardwick & Dave Muirhead for their comments
46 helping to refine and improve the manuscript. Special thanks go to Kofi Owusu for his
47 comments and assistance in modelling remotely during a pandemic. Thanks also go to
48 colleagues at the Basin Research Group for their support and guidance.

49 **Data Availability Statement**

50 The data that support the findings of this study are available from CGG Services (Norway) AS.
51 Restrictions apply to the availability of these data, which were used under license for this
52 study. Data are available from the author(s) with the permission of CGG Services (Norway)
53 AS.

54 1. Introduction

55 The importance of understanding the subsurface temperature conditions is manifold. An
56 understanding of the isotherms may help delineate important temperature driven diagenetic
57 boundaries (Bjørlykke et al., 1989). Similarly, it is useful for petroleum exploration as it
58 informs the maturity and types of hydrocarbons to be expected from a given source rock
59 (Allen & Allen, 2013). Unlike frontier areas where the effectiveness of source rocks may be in
60 doubt, this is not a concern in the North Sea. However, understanding of the present-day
61 subsurface temperature can still prove useful in such a mature basin. An example could
62 include identification of the so called “Golden Zone” thermal window in reservoirs (Nadeau,
63 2011). Similarly, an improved understanding of subsurface temperature could assist in
64 enhanced oil recovery (EOR) such as when CO₂ saturation is used to aid recovery of heavy oils
65 by reducing the density of the latter (Davarpanah & Mirshekari, 2020). Investigations into
66 geothermal energy also benefit from improved understanding of subsurface temperature
67 conditions (Bonté et al., 2012; Fuchs & Balling, 2016). The North Sea is one of the world’s
68 most prolific and extensively studied petroleum provinces (Copestake et al., 2003; Cornford,
69 1998; Leadholm et al., 1985; Rüpke et al., 2008). Over the course of the past sixty years
70 numerous oil and gas fields have been discovered, many of which have served as the testing
71 ground for new technologies such as time lapse 4D seismic or EOR (Awan et al., 2006; Landrø
72 et al., 1999). With this history of developing and applying cutting edge methodologies, it is a
73 fitting setting to test the workflow proposed here. This paper proposes and tests a means of
74 utilising reflection seismic data to predict subsurface temperatures. Previous work has
75 demonstrated that a transform based on empirical velocity and thermal conductivity data
76 may be utilised to convert seismic velocities to thermal conductivities (Sarkar, 2020; Sarkar &

77 Huuse, 2018). The derived thermal conductivities may be used in conjunction with heatflow
78 data, either from existing open-source data or through modelling of heatflow, to determine
79 subsurface temperatures from Fourier's Law under a steady state condition. There have been
80 numerous studies of the thermal conductivities and heatflow of sediments in the northern
81 North Sea (see Table A.1) (Andrews-Speed et al., 1984; Brigaud et al., 1992; Cornelius, 1975;
82 Evans, 1977; Evans & Coleman, 1974; Houbolt & Wells, 1980; Leadholm et al., 1985).
83 However, there seems to be a hiatus in such studies in recent times. Projects such as the
84 Northern Lights carbon capture and sequestration (CCS) project (Cozier, 2019) would benefit
85 greatly from current knowledge of the subsurface thermal domain for full scale CCS.

86 *1.1 Thermal model fundamentals*

87 When considering heat in the shallow subsurface it is important to understand the sources of
88 heat. That the interior of the Earth is considerably hotter is known, with surface heatflow
89 distribution closely linked to the upper mantle (Pollack et al., 1993). However 40 % of outward
90 heatflow originates in the thin outer crust (Beardsmore & Cull, 2001). Primarily this crustal
91 heat generation is from the radioactive decay of unstable isotopes of elements such as
92 uranium, thorium and potassium (in order of heat production) (Mareschal & Jaupart, 2013).
93 This radioactive heat component is non uniform in the crust due to the variable distribution
94 of radioisotope bearing lithologies within the crust. Oceanic crust for example lacks acidic
95 rocks, which tend to have the highest radioactive heat production, and thus oceanic heatflow
96 has a lower internal heat component (Hasterok et al., 2011). To a lesser extent crustal heating
97 might arise from the frictional heating at faults or from metamorphic processes, which can be
98 either endo- or exothermic in nature (Beardsmore & Cull, 2001).

99 Fluid movement in the subsurface can lead to heatflow perturbations, particularly in young
100 oceanic crust (Lister, 1972). This might be mitigated by either having sufficient sediment cover
101 or distance from the nearest seamount (from where such hydrothermal fluid systems are
102 likely to originate) (Hasterok et al., 2011). Sediment cover and high rates of sedimentation
103 might also impact heatflow conditions in terms of sediment compaction and thermal rebound
104 with corresponding lower heatflow and suppressed thermal gradient seen in locations of high
105 sediment discharge such as the Bay of Bengal (Hasterok et al., 2011).

106 To understand how subsurface temperature might be modelled in the present day it is
107 important to establish the key thermal boundary conditions and properties. These are
108 heatflow, seabed temperature, thermal conductivity, the resultant geothermal gradient, and
109 subsurface temperature. The link between heatflow, thermal conductivity and geothermal
110 gradient can be represented by the 1D approximation of Fourier's Law (Eq. 1).

111 **Equation 1:** $q = k \times \frac{dT}{dZ}$

112 Where q is heatflow (mW m^{-2}); k is thermal conductivity ($\text{W m}^{-1} \text{K}^{-1}$) and dT/dZ is geothermal
113 gradient ($^{\circ}\text{C km}^{-1}$) where Z is positive downwards. To estimate the temperature at a certain
114 depth in the subsurface, the rate of change of temperature with depth, i.e. the geothermal
115 gradient is important. It becomes apparent then that by rearranging Eq. 1, the input
116 parameters necessary to estimate this are heatflow and thermal conductivity.

117 **Equation 2:** $\frac{dT}{dZ} = \frac{q}{k}$

118 Thermal conductivity is a measure of the ease with which heat may be conducted through a
119 material (Popov et al., 2003) and is thus critical to estimating the thermal structure of the
120 subsurface. Thermal conductivity data from direct measurements are made either in situ
121 through well logs or via direct measurements on recovered samples (Andrews-Speed et al.,

122 1984; Jorand et al., 2015; Schön, 2015a). Measuring tools include either a needle probe
123 inserted into a sample or a divided bar apparatus (Evans, 1977; Horai, 1982). However, these
124 measurements may suffer from issues that affect both their ease of acquisition and reliability.
125 For example thermal conductivity probes may have poor contact with borehole walls, or the
126 needle probe reading might be affected by the alignment of the mineral fabric (anisotropy) in
127 relation to the needle orientation (Lucazeau et al., 2004; Pribnow et al., 2000). In the case of
128 the divided bar apparatus, sample preparation is a more involved process, with the
129 application of axial load equivalent to hundreds of metres of overburden on samples having
130 the effect of increasing measurements on both dry and saturated samples (Galson et al.,
131 1987). A range of downhole measuring tools may be used to measure thermal conductivity
132 within the borehole however these are discontinuous measurements that are uneconomic
133 (Mielke et al., 2017). As a result there has been considerable thought put towards deriving
134 thermal conductivity from other more easily measured physical properties such as bulk
135 density, porosity or compressional sound wave velocity (Boulanouar et al., 2013; Esteban et
136 al., 2015; Grevemeyer & Villinger, 2001; Gu et al., 2017; Hartmann et al., 2005; Horai, 1982;
137 Jorand et al., 2015). In the case of velocity, it is found to have similar sensitivity to properties
138 as thermal conductivity (Houbolt & Wells, 1980). That is, thermal conductivity is primarily
139 affected by the mineral composition, porosity and presence of fractures (Mielke et al., 2017;
140 Pimienta et al., 2018; Zamora et al., 1993). Temperature and pressure also impact thermal
141 conductivity though not as much as the other factors (Leadholm et al., 1985; Lee, 2003).

142 **Figure 1: Study area overview**

143 2. Geological history

144 The North Viking Graben (NVG) (Fig. 1) is located in the Northern North Sea between the East
145 Shetland Platform to the West and the Horda Platform to the east, and part of the north
146 western European cratonic block (Brigaud et al., 1992). It is part of the North Sea Graben
147 system (Fig. 2) (Cornford, 1998). It is a Mesozoic rift system, with the rifting in this area having
148 occurred after the Caledonian orogeny (and extensional orogenic collapse), with there being
149 two primary phases of extensional rifting since the Devonian (Fichler et al., 2011; Rüpke et
150 al., 2008; Ziegler, 1992). Primary rifting in the Permian to Early Triassic was followed by a post
151 rift subsidence period (Nøttvedt et al., 1995). The next phase of rifting was from mid Jurassic
152 to early Cretaceous and was also followed by a post rift subsidence period. The rift axis for
153 the Permo-Triassic rifting is believed to be located under the present Horda Platform with the
154 late Jurassic rift axis below the present day Viking Graben (Christiansson et al., 2000). No
155 major tectonic activity is believed to have occurred post Jurassic though there is some
156 conjecture regarding a Tertiary rifting episode (Rüpke et al., 2008) and mid Miocene inversion
157 (Løseth et al., 2013, 2016). The predominant rift direction in the N to NE striking Viking Graben
158 was west-east and northwest-southeast.

159 The sedimentary record in this area is Devonian and younger. Sand and shales dominate the
160 Triassic to Jurassic basin fill with carbonates and shales predominant in the Cretaceous
161 (Brigaud et al., 1992). Tertiary lithologies consist of shales, silts and sands, with a brief period
162 of Paleocene volcanism marked by the widespread deposition of volcanic tuffs across the
163 basin (Haaland et al., 2000). Crustal basement rocks in this area have a history exceeding one
164 Wilson cycle and trace back to the junction between the Laurentian and Baltican plates,
165 including the opening of the Iapetus Ocean, island arc development linked to oceanic

166 subduction and the Caledonian orogeny (Fossen et al., 2008; Meert & Torsvik, 2003). The
167 composition of the basement rocks can be seen to vary from granites underneath the East
168 Shetland Platform to low and intermediate grade metamorphic and metamorphosed
169 sediments below the Viking Graben and Horda Platform (Fichler et al., 2011).
170 Source rocks in the area are predominantly Kimmeridge Clay (shales) that were deposited in
171 the Late Jurassic (Davison & Underhill, 2012; Gautier, 2005). Abundant reservoir rocks are
172 available in the NVG all of which exist with a variety of trapping mechanisms. These pre rift
173 reservoirs are usually found in tilted fault blocks where fine-grained post rift sedimentary
174 sequences act as seals.

175 **Figure 2: Structural transect**

176 3. Data

177 The dataset used for the study includes reflection seismic and borehole data.

178 The North Viking Graben ‘mega-merge’ was acquired by CGG between 2014 and 2016,
179 covering a total area of 35410 km². This broadband 3D seismic reflection survey of BroadSeis™
180 and BroadSource™ configuration covers the northern North Sea basin and was shot in a north-
181 south direction, recorded in TWT down to 9 seconds with an acquisition sample interval of 2
182 ms (Purvis et al., 2018) though for this work the pre-stack depth migrated (PSDM) volume in
183 the depth domain was utilised. The volume has an inline and crossline bin spacing of 6.25 x
184 18.75 m. A (flip flop) shot point interval of 18.75 m and a source separation of 37.5 m gives a
185 nominal common-mid-point (CMP) fold of 106. Twelve streamers were used in total, each
186 7950 m long, with 636 channels towed at depths of 7 – 50 m (BroadSeis™ profile).

187 Multiple algorithms were used to remove noise and multiples. Both manual picking and time
188 tomographic inversion (TOMOT) was used to generate velocities with imaging done using

189 Kirchhoff PSTM. A proprietary CGG methodology of continuous automatic bi-spectral velocity
190 picking helped generate the final stacking velocities (Purvis et al., 2018). The processed PSTM
191 and PSDM cubes underpin the modelling work conducted in this study.

192 The full waveform inversion (FWI) technique aims to produce a high-fidelity subsurface
193 representation of velocity, as the velocity model minimises differences between observed
194 and modelled seismic waveforms within the original raw data (Warner et al., 2013). In making
195 the FWI velocity product, a best guess starting model based on seismic processing velocities
196 is iteratively improved using a sequence of linearized local inversions (Warner et al., 2013).
197 For the CGG NVG survey the fast track velocity product was made from the Dix conversion of
198 root mean squared (RMS) stacking velocities, followed by Kirchhoff depth migration to
199 residual move out (RMO) velocities (CGG, 2019). During the FWI process, the model was
200 subdivided into smaller areas targeting regions of key geology, allowing verification to be
201 conducted (CGG, 2019). Three production runs at ever increasing seismic frequency (4; 5.5 &
202 8 Hz) were conducted as part of the FWI model build (CGG, 2019). The final 8 Hz update
203 produced the velocity model that best follows geological structure and can characterise small
204 scale features such as injectites (CGG, 2019). The FWI model was calibrated using 101 wells
205 with QC checks completed against sonic log data (CGG, 2019).

206 Borehole data for this study were primarily sourced from the Norwegian Petroleum
207 Directorate (NPD) website. This gave access to well reports, mud logs, geological reports, and
208 wireline logging data. Because the FWI volume was already calibrated against downhole sonic
209 velocity data and provided in the depth domain, the primary data of interest for this study
210 were the corrected bottom hole temperatures (BHT) recorded for each well within the
211 thermal model area. Where drill stem test temperature readings are available these have
212 been used in the NPD dataset. Publicly available heatflow data from the International

213 Heatflow Commission (IHFC) database were used to provide constraint on the heatflow
214 parameter (Gosnold & Panda, 2002). There is a scarcity of data points covering the model
215 area as seen in Fig. 1b with the nearest offshore data point too distant to confidently
216 interpolate from (Ritter et al., 2004).

217 4. Methods

218 The modelling work has been conducted using Schlumberger's Petrel software used for 3D
219 seismic interpretation and to create and manipulate the property volumes and thermal
220 models in this work. Standard seismic interpretation techniques (Cox et al., 2020;
221 Posamentier, 2004), including horizon mapping, surface map creation and seismic attribute
222 extractions were conducted for a structural interpretation of two reference horizons, the
223 seafloor and the Base Cretaceous Unconformity (BCU). The BCU follows the regional
224 stratigraphic framework and serves as a reference horizon, upon which model outputs are
225 overlain as attributes, thus giving a regional context to the results (Evans, 2003). The seafloor
226 is the ceiling for the thermal models, separating the hydrothermal and the geothermal
227 domains. Both horizons were mapped in depth using the 3D reflection seismic data. For the
228 purposes of this work, no other structural interpretation was necessary. Further
229 interpretation or import of grids can of course be done to observe the predicted temperature
230 at desired stratigraphic levels.

231 The workflow utilised in this project is summarised in Fig. 3. It can be broken down into two
232 main components: the forward modelling approach uses the seismic velocity data as the input
233 parameter to model the thermal conductivity and subsurface temperature using constant
234 surface heatflows, which in turn is calibrated against available BHT data; the inverse approach
235 calculates heatflow from the observed BHTs and the thermal conductivity structure. As

236 heatflow is an important input parameter to model temperature, it becomes possible to
237 update the temperature forward model with the inverse modelling results, and thus validate
238 the final temperature model results, in a manner akin to tomographic update of velocity
239 models (Jones, 2018; Prada et al., 2019).

240 **Figure 3: Reflection seismic thermometry workflow**

241 *4.1 Forward modelling problem – present day subsurface temperature*

242 The reflection seismic dataset is a modern broadband seismic survey covering the North
243 Viking Graben (NVG) spanning across parts of the UK and Norwegian continental shelves
244 (UKCS and NCS, respectively). The full waveform inversion (FWI) final velocity model is the
245 key reflection seismic data product underpinning the modelling work.

246 *4.1.1 Thermal conductivity structure*

247 This study uses a high-resolution 3D seismic velocity volume and experimental data relating
248 velocity and conductivity with an empirical relationship (Fig. 4). As this project outlines a
249 remote sensing method, direct thermal conductivity measurement is not possible and instead
250 it must be indirectly determined. If the rocks of the subsurface are considered as a multi
251 component system comprised of minerals, texture (of grains, such as their shape and size),
252 porosity and the fluid content, it becomes possible in an ideal scenario to determine the
253 composite effective thermal conductivity from the contribution of each component part using
254 a suitable mixing law or effective medium model (Duffaut et al., 2018; Hartmann et al., 2005;
255 Schön, 2015b). Normally mud logging data (available here from the NPD database) would be
256 utilised to determine the volumetric fraction of each mineral (Brigaud et al., 1990). We,
257 however, are presenting a remote sensing scenario where only the temperature data from
258 wells is being used to correlate the predicted temperatures with.

259 The elastic properties of the subsurface are well constrained from seismic data (Mavko et al.,
260 2009) and it provides the avenue to the desired thermal structure. To link thermal properties
261 (thermal conductivity) to elastic properties (acoustic velocity), knowledge of their primary
262 controls becomes necessary. Experimental work has shown that these controls include
263 mineral composition, texture, porosity, the presence of fractures and fluid fill (Gegenhuber &

264 Schoen, 2012). It helps to think of porosity as the crucial intermediary in the proposed
265 empirical relationship as there have been studies examining the link between acoustic
266 velocity and porosity (Eberhart-Phillips et al., 1989; Lee, 2003; Velde, 1996); and similarly the
267 relationship between porosity and thermal conductivity (Fuchs & Förster, 2013; Jorand et al.,
268 2015). By making the direct leap it must be noted that there are inherent assumptions in such
269 an approach. One concern that may arise is the extent to which the variation in the velocity
270 signal solely corresponding to a thermal conductivity variation (as desired) or is it in fact
271 influenced by external factors (for example fluid overpressure). In such an instance, this issue
272 may be obviated by restricting application to regions of hydrostatic fluid pressure only,
273 however it might be the case that slight overpressure would only correspond to a minor
274 increase in velocity (Lee, 2003). While porosity is a crucial intermediary, mineral composition
275 has a dominant impact on thermal conductivity. Argillaceous rocks have lower conductivities
276 than non-argillaceous (quartz rich) rocks for example (Mavko et al., 2009). The more
277 monomineralic a rock, the greater the correlation between velocity and thermal conductivity
278 (Esteban et al., 2015), which alludes to the impact of anisotropy of thermal conductivity.
279 When considering clay rich rocks, they display poorer correlations for thermal conductivity
280 arising from the platy nature of clay grains (versus more rounded sand grains). At greater
281 compaction however, parallel alignment of clay grains could contribute towards lower
282 effective porosities and thus a stronger correlation with both velocity and thermal
283 conductivity (Velde, 1996). With use of this proposed empirical transform expected for both
284 shallow and deep intervals, it is hoped that the variability of clay rich sediment at shallow
285 levels is balanced at deeper levels.

286 It must be noted that even the best thermal conductivity models are subject to caveats, either
287 in the form of the inherent assumptions or the specific circumstances where direct
288 relationships might not be as strong.

289 By including a wide range of studies, covering a wide array of lithologies and settings, it is
290 hoped that the resulting empirical relationship can serve as a robust first order estimate for
291 the varying porosities encountered within any projected study area. Lithologies include clastic
292 sediments (sandstones of varying grain size from fine to coarse; varying mineral content
293 including nearly isotropic clean quartz rich sandstones & clay rich sandstones); carbonates
294 (limestone; dolomite; marl; etc); mudstones (clay- & siltstones); and volcanic & granitic rocks
295 (granite; basalt; gabbro; etc). The sample dataset is limited to wet samples only and
296 measurements taken using transient measurement apparatus such as the optical scanning
297 method (Popov et al., 1999), in order to maintain applicability to fluid filled rocks in the
298 subsurface and parity between data points respectively. Though the study area is dominated
299 by shales, the approach adopted with the empirical relationship is intended to be globally
300 applicable and thus incorporates samples not proportionally dominant in the NVG study. This
301 approach has previously been applied in passive margin settings offshore Namibia and
302 offshore USA (Sarkar & Huuse, 2018, 2021). Future studies could aim to utilise an edited
303 sample list reflective of the dominant lithologies in the target area. The best fit regression
304 (Fig. 4) through the subset of points is as follows:

305 **Equation 3:** $k_V = (6 \times 10^{-5})V_p^{1.3279}$

306 Where k_V is thermal conductivity from velocity ($W m^{-1} K^{-1}$) and V_p is P wave velocity ($m s^{-1}$)

307 **Figure 4:** Empirical transform for velocity and thermal conductivity

308 With a highly detailed FWI velocity volume representing the P-wave velocity of the subsurface
309 and a function relating velocity and thermal conductivity, it is possible to convert the FWI
310 velocity volume into a volume of thermal conductivity varying with depth (using Eq. 3). To
311 facilitate the workflow the FWI interval velocity volume was first converted to an average
312 velocity volume in depth below the seabed (as the geotherm starts at seabed) and this in turn
313 allowed the estimation of instantaneous average thermal conductivity as a function of depth
314 in the entire volume.

315 *4.1.2 Heatflow input scenarios*

316 In order to determine the geothermal gradient (Eq. 2), information regarding the heatflow in
317 the study area is required alongside thermal conductivity.

318 A priori heatflow values were defined based on a combination of existing literature and data
319 from the IHFC. As seen on Fig. 1b, there is a paucity of IHFC data points in the study area. This
320 leads to examining the published record for maps of heatflow covering the North Sea, and
321 these tend to exist in the form of heatflow estimate grids at regional or global scale. Examining
322 these grids such as Davies (2013) or Lucazeau (2019), it becomes apparent that the heatflow
323 varies greatly at basin scale. This seems to depend not just on the size of the grid squares over
324 which the authors have applied their interpolation, but the exact technique used to
325 interpolate and the input parameters they have used will lead to this variability. Consequently
326 it was decided that analysis of the range of heatflow values that are observed in the literature
327 for this area (Andrews-Speed et al., 1984; Cornelius, 1975; Davies, 2013; Evans & Coleman,
328 1974; Harper, 1971; Leadholm et al., 1985; Lucazeau, 2019; Ritter et al., 2004) will be used to
329 define predetermined starting conditions for heatflow. By using the conclusions of these
330 existing studies, previous modelling accounting for factors such as the impact of the Curie

331 depth in the area or the impact of basal heatflow, is incorporated. This gives a low-, mid- and
332 high- case a priori surface heatflow of 60, 70 and 80 mW m⁻² respectively.

333 *4.1.3 Temperature grids & calibration*

334 Having determined thermal conductivity and established heatflow scenarios it becomes
335 possible to calculate three geothermal gradient scenarios for the model area. By convolving
336 this with the subsurface depth and incorporating the bottom water temperature (BWT) (i.e.,
337 seabed temperature) an estimate of present-day subsurface temperature can be made.

338 **Equation 4:** $T = T_{SEABED} + \left(\frac{dT}{dZ} \times Z_{SUBSURFACE}\right)$

339 where T is predicted temperature (°C); T_{SEABED} is the temperature at seabed (°C); dT/dZ is the
340 instantaneous geothermal gradient (°C km⁻¹) (Eq. 2); and $Z_{SUBSURFACE}$ is the subsurface depth
341 (km).

342 Early studies into the geothermal aspects of the North Sea would set temperature at the
343 seafloor to a constant, for example 10 °C (Cornelius, 1975; Evans & Coleman, 1974; Harper,
344 1971). Here however seafloor temperature was assigned through decadal averages from the
345 World Ocean Atlas (WOA) dataset (Boyer et al., 2014; Locarnini et al., 2013). Using the nearest
346 measurement node from the 0.25-degree grid of the WOA dataset, the temperature profile
347 (hydrothermal gradient) for this was used to interpolate seafloor temperatures across the
348 seafloor within the model area. Temperatures are found to be in the range of 6 to 9 °C with
349 seafloor temperatures in the shallower water of the UKCS averaging 7.3 °C, and in the
350 relatively deeper waters to the east, these temperatures average 8.7 °C. By basing the
351 seafloor temperatures on a decadal average, the variability of seasonal bottom water
352 conditions and longer scale variability will be negated. This gives a baseline temperature from

353 which the well readings can be seen in context to, particularly with regard to determining the
354 geothermal gradient.

355 Thermograms, or temperature profiles, depicting temperature change with depth are one
356 way of displaying the model results for each well site (Cornelius, 1975). Petrel allows for the
357 creation of synthetic logs from a reservoir model or pillar grid. This requires resampling the
358 temperature models into a pillar grid coincident with the extent of the area of interest. The
359 dimensions of the individual cells of the grid, and subsequently the total number of cells
360 constituting the entire grid are important with respect to the total compute power. The
361 modelling results displayed here have a lateral resolution of 50*50 m (XY orientation), with
362 the top of the model coinciding with mean sea level (MSL) and the base being set at 5.5 km
363 depth. It is important to establish the base for the thermal model as this will define the
364 interval over which geothermal gradient is calculated. This basal depth encompasses the
365 maximum vertical depth of the wells used for calibration. Cell height was set to 20 m, in
366 accordance with the vertical resolution of the velocity data. For these dimensions, the entire
367 gridded model comprises about 1.4 billion voxels.

368 With all the input and derived seismic attributes resampled as properties in the pillar grid,
369 synthetic logs for each well are generated. These synthetic logs are made for the three
370 temperature prediction volumes coincident with the three heatflow input scenarios. The
371 estimated temperature at the bottom of each well from the synthetic logs is then plotted
372 against the recorded corrected BHT (Fig. 7). Theoretically, the misfit between observed and
373 modelled temperature for each well can be used to calculate how much the heatflow input
374 for each well must be adjusted for there to be no misfit. In this way, the most representative
375 heatflow value for the area might be calibrated.

4.2 Inverse modelling problem – solving for heatflow

The first stage of subsurface temperature modelling assumed 3 discrete heatflow parameter input scenarios. In this instance, discrete values for heatflow across the model area were used to simulate each temperature scenario. However, heatflow is likely not homogeneous across the model area and there may be lateral variability across individual structures and preferred fluid migration paths. If recorded temperatures in the wells are assumed to be correct and with knowledge of the seafloor temperature, geothermal gradient can be independently computed for each well site. Additionally, if the seismic velocity derived thermal conductivity is considered valid, it becomes possible to use the 1D approximation of Fourier's Law to derive heatflow at each well location. This is the inverse problem.

Equation 5:
$$q = K_V \times \left(\frac{T_{BHT} - T_{SEAFLOOR}}{dZ} \right)$$

Where q is heatflow (mW m^{-2}); K_V is thermal conductivity from velocity ($\text{W m}^{-1} \text{K}^{-1}$); T_{BHT} is bottom hole temperature ($^{\circ}\text{C}$); $T_{SEAFLOOR}$ is temperature at seafloor ($^{\circ}\text{C}$); and dZ is the vertical depth interval (km).

Interpolating for heatflow between the wells creates a map of inversely modelled laterally varying heatflow. An inverse distance weighting (IDW) function has been used to interpolate heatflow. The values of cells in the vicinity of the processing cell (interpolated gap) are averaged, with the distance of the neighbouring cell having an inverse weighting (Watson & Philip, 1985).

4.3 Final temperature model

Calibrating the results of the temperature forward model with the different heatflow input scenarios, it is likely to show different degrees of agreement. Iteratively updating the heatflow

398 parameter input each time and remodelling for subsurface temperature should theoretically
399 permit the most representative heatflow across the study area to be arrived at ultimately.
400 However, this former approach was not pursued as it was shown previously that inverse
401 modelling (see section 4.2) allows the determination of laterally varying heatflow across the
402 model area. Convolving this heatflow with the seismically derived thermal conductivity (Eq.
403 2), it should be possible to generate a volume of instantaneous geothermal gradient that has
404 most agreement across all the calibration wells. This thermal gradient is used to generate a
405 final temperature model (Eq. 4) that is resampled into the pillar grid and used to output
406 synthetic temperature logs. Predicted temperature from these logs at hole bottom is
407 extracted and used to calibrate against recorded BHT as before.

408 The well 31/5-7 is located due southwest of Troll A field and targets the lower Jurassic Cook
409 and Johanssen formations for injection. The targeted interval has ca.173 m of sandstone
410 overlain by 75 m of shale acting as a seal above it. Pressure data indicates no communication
411 in rocks above and below the shale, reinforcing its seal properties. With no results from this
412 well published due to its very recent completion, it was decided to use the available details
413 (well head coordinates and total depth) to simulate the temperature profile for this well using
414 our model.

415 5. Results

416 The results from the modelling work are presented either as seismic attribute overlays on
417 transects or by means of attribute maps on a gridded horizon. But for the purposes of
418 calibration the primary output is the synthetic temperature log data from the wells. These
419 results are discussed individually in the following section.

420 The FWI interval velocity volume was converted to an average velocity volume, before
421 applying the velocity to thermal conductivity transform (Fig. 4) to produce a volume of
422 average thermal conductivity. Looking at the internal velocity derived thermal conductivity
423 structure (Fig. 5b), the direct nature of the bulk shift results in the thermal conductivity
424 variation with depth across the volume corresponding to the level of detail seen in the input
425 velocity (Fig. 5a). Cretaceous and younger Cenozoic sediment cover is seen to have relatively
426 low thermal conductivities, with a distinct increase in thermal conductivity seen in the tilted
427 fault blocks of the Viking Graben. The graben corresponds with the greatest amount of
428 overlying sediment cover and lower conductivities relative to the neighbouring rift shoulder.

429 **Figure 5: Derived thermal conductivity structure**

430 The forward modelling results using the predefined heatflow input scenarios are displayed on
431 the west-east transect A-A' (see Fig. 6). As expected, temperatures increase gradually with
432 depth, with no major anomalous zones seen. Cenozoic sediments are coolest with the highest
433 temperatures in the graben itself, which makes sense considering constant heatflow but
434 lower conductivities of the sediments within the graben. Isotherms are more widely spaced
435 as we move towards the Horda Platform in the east where the conductivity is greater. As
436 predicted by Fourier's Law, increasing heatflow leads to increased subsurface temperatures.
437 The direct impact of each heatflow input scenario is better visualised when cross plotting the
438 temperature extracted from each well (Fig. 7).

439 **Figure 6: Forward modelling output for heatflow scenarios**

440 As stated earlier, synthetic thermograms corresponding to the well path of each calibration
441 well were extracted from the predicted temperature models. The temperature at bottom
442 hole in each case has been plotted against the recorded BHT. The best fit regression through
443 each cluster of points and the gradient of this is used as a measure of the degree of agreement

444 between predicted and observed values. The R-squared value, a measure of statistical validity
445 for each regression line, for all three heatflow scenarios is above the 0.7 that is regarded as
446 being the threshold for statistical reliability. Analysing the misfit between predicted BHT and
447 corrected BHT, it is found that on average the low heatflow scenario is 0.64 °C cooler; the mid
448 heatflow scenario has average misfit 15.4 °C higher and the high heatflow scenario has an
449 average misfit of 31.3 °C higher. With increasing heatflow, the corresponding gradient of the
450 regression line through that cluster of points also increases, as does the Y-intercept. The
451 optimum desired gradient that would be expected for best agreement between predicted
452 and observed temperatures would verge on 1, and from this initial forward modelling it is
453 seen that the lowest heatflow scenario is closest to this. However, it is also the case that the
454 optimum regression should be seen to pass through the origin of the cross plot and increasing
455 the heatflow moves each regression further away from this.

456 **Figure 7: Forward modelling results calibrated**

457 When deriving ocean bottom heatflow across the model area through an inverse modelling
458 problem (see 4.2) (Fig. 8), gives mean heatflow of 60.05 mW m⁻² and a median of 62.82 mW
459 m⁻². The effective range of heatflow is between 40 to 70 mW m⁻². Observing the heatflow
460 variation across the area (Fig 8) certain wells are seen to have much lower heatflow than their
461 immediate vicinity. Consequently, during interpolation, these wells are seen in a bulls-eye
462 zone of depressed heatflow. The most prominent of these is observed to the southwest, with
463 two wells (30/5-1 & 30/8-2) having depressed effective heatflow. Referring to Fig. 1 these two
464 wells do not coincide with any field. The other prominent heatflow depression is found to the
465 northeast of the model area at the intersection between Troll-A and Troll-B. The north-
466 westernmost and easternmost wells (29/3-1 & 32/4-1, respectively) (Fig. 8) influence the
467 immediate vicinity by elevating the heatflow interpolated here.

468 **Figure 8: Inverse modelling of heatflow and results**

469 The result of running a final iteration of forward modelling for temperature with the
470 continually laterally varying heatflow derived in Fig. 8 is shown in Fig. 9. We find when cross
471 plotting predicted temperatures from this final model against BHT that the general
472 distribution of points has a far tighter spread than in the previous modelling instances. The
473 average misfit between predicted BHT and measured BHT is 0.58 °C. Furthermore, the best
474 fit regression through this set of points has a gradient nearly equal to 1, and passes nearest
475 to the origin, as is expected for the model best reflecting the actual subsurface temperature.
476 Interestingly, the average of the inverse modelled heatflow as stated earlier is nearly equal
477 to the low case heatflow input scenario used in the early-stage forward modelling. Looking at
478 the distribution of well points (Fig. 9) however it is clear that there is a great disparity in the
479 two approaches. The visual impact of the two approaches is shown in Fig. 10d, e.

480 **Figure 9: Well calibration including final temperature model**

481 The result from the final iteration of the temperature model overlain with key structures is
482 shown in Fig. 10a. Running an RMS amplitude extraction for thermal conductivity on a
483 reference horizon (Fig. 10c), in this case the BCU, it is observed that the highest thermal
484 conductivities are observed in the heart of the Viking Graben, where the BCU is deepest (Fig.
485 10b). On the flanks of the graben and eastward towards the Horda Platform, thermal
486 conductivities are seen to decrease considerably, consistent with the increasingly shallowing
487 BCU surface at that point. Reverting to the temperature model outputs, we see the difference
488 between the initial forward modelling approach (Fig. 10d) and the final inverse modelled
489 heatflow influenced iteration (Fig. 10e). Comparing the temperatures, within the deep graben
490 for example, it is immediately apparent there is greater variation and detail discernible in
491 from this latter approach. Indeed, what is seen is that some anomalous temperature zones

492 are seen in this final iteration at the northern tip of the Troll field that seem to directly
493 correlate with the anomalous heatflow zone from the interpolation (see Fig. 8a).

494 **Figure 10: Temperature modelling results**

495 The results of simulating the thermal profile for the Northern Lights well 31/5-7 (Eos) are
496 shown in Fig. 11, with temperature at bottom hole of 97 °C falling well within the projected
497 100 °C range published on the project website (see: <https://northernlightsccs.com/en/about>
498 accessed at 25/07/2020). Data released by Equinor and the Norwegian government in
499 October 2020 with preliminary results indicated temperature at the bottom of 103 °C. The
500 final well report with its BHT record has not yet been made public but preliminary results from
501 the 31/5-7 prediction show a good agreement between model prediction and reality.

502 **Figure 11: CCS well 31/5-7 modelled**

503 **6. Discussion**

504 There are multiple corollaries of modelling for subsurface temperature in this manner. The
505 seismic led method of deriving subsurface thermal conductivity structure should enable the
506 verification of zones of thermal blanketing (Cercione & Pollack, 1991; Wangen, 1995). Due to
507 the direct relationship between velocity and thermal conductivity as used here, any zones of
508 anomalously high or low velocity will be reflected in thermal conductivity anomalies. The
509 general trend contains lithologies such as sandstone, shale, limestone and crystalline rocks.
510 This excludes lithologies that deviate from our general trend such as halite, which will need
511 to be considered explicitly to represent the temperature above, within and below such
512 anomalous bodies.

513 The benefit of the highly detailed FWI velocity model available in this area is that the velocity
514 data has been calibrated against wells in the NVG, thus ensuring the velocity model is a good

515 representation of true subsurface properties and conditions. The conversion to thermal
516 conductivity and temperature provides another means of visualising the subsurface. It is of
517 critical importance to both petroleum exploration and carbon sequestration in the area. In
518 other locations such estimates would be highly beneficial to geothermal or gas storage
519 operations. It must be noted that any artefacts in the velocity data will be translated to the
520 derived thermal conductivity, instantaneous geothermal gradient and predicted temperature
521 volumes as a consequence of the direct transitions in the workflow.

522 *6.1 Heatflow modelling – impact and implications*

523 The validation of the inverse modelling of heatflow as an input as opposed to the use of a
524 discrete integer value heatflow input is borne out by the results. The interpolation of heatflow
525 over the 12000 km² model area (Fig. 8) highlights the variation in heatflow magnitude laterally
526 at improved coverage compared to most existing studies. As shown earlier (Fig. 1), global and
527 regional compilations usually produce heatflow grids that are at the scale of 1-degree grid
528 squares or larger. The lateral resolution is thus many orders of magnitude poorer than when
529 based on BHT and conductivity data. Interpolating heatflow at such fine scale might enable
530 the examination of any trends, if any, in heatflow versus features that may be hydrocarbon
531 fields, or structural trends (for example major fault networks). While there is a paucity of data
532 points in the IHFC grid coinciding with large parts of the Northern and Central North Sea, the
533 many decades of hydrocarbon exploration in the area led to numerous wells, many of which
534 have detailed records of BHT. When combined with the seismic velocity driven model to
535 ascertain thermal conductivity structure, it should allow for the possibility to fill in the large
536 gaps in the global point heatflow database, which in turn should allow for more detailed basin
537 scale heatflow studies.

538 The thermal anomaly visible in the interpolated ocean bottom surface heatflow map (Fig. 8)
539 can be seen to coincide with the Troll Field (Fig. 1). Records of this thermal anomaly attribute
540 it to transient effects of uplift caused by late Quaternary deglaciation (Cornford, 1998). The
541 method used to interpolate heatflow might have an impact. IDW gives the best results when
542 the sampling is sufficiently dense with respect to the local variation being simulated (Watson
543 & Philip, 1985). Where sampling is sparse or uneven, the interpolated result will insufficiently
544 represent the desired surface (Philip & Watson, 1982). From the density of wells around
545 existing fields in the area, we can be sure that the IDW interpolation will reliably capture the
546 laterally varying heatflow at this local scale. Nonetheless at the edges of the model area there
547 will be some degree of uncertainty associated with the interpolated heatflow, a consequence
548 of the sampling sparseness in these regions. Kriging would be a more statistically rigorous
549 method of interpolating heatflow, but it requires a prior investigation of the spatial behaviour
550 of heatflow in the sample points. This is incumbent on a pre-existing understanding of the
551 factors influencing the modelled parameter. In a blind test the latter would not necessarily be
552 possible, and thus IDW should be satisfactory for a first order interpretation.

553 While heatflow has been derived from inverse modelling, in sedimentary basins there is a
554 thermal contribution linked to the radiogenic heat production of sediments and crustal
555 material, and the contribution of heat from the earth's deep interior (that is mantle) (Allen &
556 Allen, 2013; Hasterok et al., 2011; Hasterok, 2010; Hokstad et al., 2017). The modelling here
557 estimated present-day subsurface temperatures using a steady state approximation (Eq. 1).
558 As such, a conscious decision was made to introduce as few variables as possible. Radiogenic
559 heat production would be one such variable. Its impact here has been noted but not explicitly
560 modelled. Mantle heat production is usually estimated from the Moho, whose depth in the
561 area averages roughly 30 km (Grad & Tiira, 2009). Estimates of the Curie isotherm at its

562 shallowest in the study area place it at similar average depths of ca.30 km (Fichler et al., 2011;
563 Kubala et al., 2003). Under the graben, Moho depth does become shallow, up to 22 km in
564 places (Licciardi et al., 2020). Referring to Fig. 8a, modelled heatflow is higher towards the
565 graben centre, which suggests some correlation. With the thermal model base set at 5.5 km,
566 and the degree of shallowing of the Moho not exceeding ~22 km at its shallowest point, the
567 impact of mantle heat input from a modelling perspective is considered negligible in this
568 instance. The general Moho trend in the northern North Sea has a gradual shallowing in the
569 north-west, near the Shetland Islands (Licciardi et al., 2020). If conducting thermal modelling
570 over the whole NVG survey area, and with the basal limits for the model set sufficiently deep
571 such that there might be a basal mantle heatflow effect due to proximity to the Moho for the
572 deepest section of the model. Future models seeking to integrate surface heatflow with a
573 basal heatflow flux can rely on the Curie depth for constraint (Blakely, 1988). The Curie depth
574 is often seen to coincide with a compositional boundary reflecting the loss of magnetic
575 minerals in rocks (Rajaram et al., 2009) and thus can be treated as an isotherm, identifiable
576 using magnetic geophysical methods. It should become possible then to contrast modelled
577 surface heatflow against calculated surface heatflow from past studies, allowing
578 determination of whether the sensitivity of NVG thermal anomalies is to basal flux or thermal
579 conductivity effects, or a combination of the two factors.

580 *6.2 Relevance*

581 The applications of this proposed workflow range from immediate usage by the hydrocarbon
582 industry to supporting new subsurface uses aligned with the energy transition. Hydrocarbon
583 explorationists may use the knowledge of the isotherms to help develop their petroleum
584 systems models or it can help production teams better ascertain the distribution of

585 temperature in the reservoir in order to inform reservoir engineering projects to maximise
586 recovery. Knowledge of subsurface thermal structure is important for the nuclear waste
587 disposal industry due to the sensitivity of the waste to thermal perturbations (Brigaud et al.,
588 1992). From a low carbon technology solutions perspective, mapping subsurface isotherms
589 may enable geothermal energy prospecting and the understanding of subsurface
590 temperature will be important for CCS operations in both frontier and mature basins.

591 Simulating temperatures for the current CCS Northern Lights well 31/5-7 emphasises the real-
592 world applicability of this model, both in terms of its speed of producing an estimate and its
593 relevance in the energy transition for the future. It is important to understand the
594 temperature conditions in CO₂ storage reservoirs as the properties of the gas vary with
595 temperature and pressure. Of these only the pressure is routinely estimated based on seismic
596 data (Eiken et al., 2011). At higher temperatures the density of CO₂ decreases, theoretically
597 allowing for a greater volume of it to be stored in a reservoir. Studies of CO₂ injection into the
598 Utsira formation (part of the Sleipner Project) have shown that reservoir temperature is a
599 source of uncertainty as it can also impact the diffusivity of the gas within the reservoir
600 (Chadwick et al., 2006). By using the subsurface thermal model proposed here, this key
601 uncertainty may be constrained by project planners, both giving more constraint on the
602 volume of CO₂ able to be sequestered within a reservoir, but also the ability to ascertain
603 lateral temperature variability would enable more nuanced storage across different parts of
604 a reservoir. Finally understanding the temperature conditions and where the potential of CO₂
605 diffusivity is highest could help mitigate the possibility of CO₂ leakage.

606 It is not just industrial applications for which this methodology may be utilised. Academic end
607 use cases are also envisioned. The study of the microorganisms endemic to the deep
608 subsurface is nascent and opens up the possibility of the crust playing host to potentially great

609 biodiversity and biomass (Basso et al., 2005). Limited studies into the microbial organisms
610 found in oil reservoirs have yielded surprising results. One such study in the Troll field,
611 examining the microbial diversity of produced water, indicated that these microbes were not
612 introduced as contaminants into the reservoir as a by-product of drilling; instead RNA
613 analyses and gene matching has indicated that these are a distinct genera of temperature
614 sensitive microbes that do not match existing known mesophiles or thermophiles (Dahle et
615 al., 2008). Due to the temperature dependence of these novel microbes, and the difficulty
616 with sampling, an understanding of subsurface conditions might help in providing some
617 inclination of the exact genera that can be encountered in a reservoir based on the predicted
618 temperatures from the model. Thus, it is envisioned that the proposed model can assist the
619 microbiological community as well. Bacterial remediation has been studied as a means of
620 clean up for chemical or hydrocarbon contaminated reservoirs or aquifers (Hazen, 1997).
621 Understanding of the temperature field in the subsurface can help determine how conducive
622 the conditions are to the proliferation of such organisms. From a resource perspective
623 microorganisms have been found to impact natural gas, carbon sequestration, hydrocarbons
624 or even interfere with the underground storage of nuclear waste (Christofi & Philip, 1997).

625 7. Conclusion

626 The work outlines a novel methodology that utilises state of the art velocity model data from
627 a mature basin such as the North Viking Graben to determine present day subsurface
628 temperatures non-invasively. Forward modelling simulations underpinned by the velocity
629 data and utilising an empirical thermal conductivity transform have been calibrated against
630 recorded temperature data from oil field wells in this sector of the North Sea. Existing work
631 using well data allows the computing of the vertical component of heatflow, in the same

632 orientation as the well. Through inverse modelling here it has been demonstrated that
633 heatflow can be computed in such a manner that lateral heatflow variability coverage is
634 improved compared to existing datasets. Using this derived heatflow to iteratively update the
635 forward model produced a temperature model, the calibration results for which indicate the
636 validity of this approach. To prove the real-world efficacy of this work it has been applied to
637 a recently drilled carbon capture and sequestration well, estimating the temperature in the
638 target reservoir to be within a 5 °C margin at ~3 km subsurface depth, highlighting the
639 usability and robustness of this methodology in hydrocarbon exploration and future energy
640 transition projects.

641 8. References

- 642 Allen, P., & Allen, J. (2013). Basin analysis: principles and application to petroleum play
643 assessment. In *WileyBlackwell*.
- 644 Andrews-Speed, C. P., Oxburgh, E. R., & Cooper, B. A. (1984). Temperatures and Depth-
645 Dependent Heat Flow in Western North Sea. *American Association of Petroleum*
646 *Geologists Bulletin*, 68(11), 1764–1781.
- 647 Awan, A. R., Teigland, R., & Kleppe, J. (2006). EOR survey in the North Sea. *Proceedings - SPE*
648 *Symposium on Improved Oil Recovery*, 1, 294–309. <https://doi.org/10.2523/99546-ms>
- 649 Basso, O., Lascourrèges, J., Jarry, M., & Magot, M. (2005). The effect of cleaning and
650 disinfecting the sampling well on the microbial communities of deep subsurface water
651 samples. *Environmental Microbiology*, 7(1), 13–21. <https://doi.org/10.1111/j.1462-2920.2004.00660.x>
- 653 Beardsmore, G., & Cull, J. (2001). Crustal Heat Flow: A Guide to Measurement and Modelling.
654 In *Cambridge University Press*. <https://doi.org/10.1017/S0016756803218021>
- 655 Becker, J. J., Sandwell, D. T., Smith, W. H. F., Braud, J., Binder, B., Depner, J., Fabre, D., Factor,
656 J., Ingalls, S., Kim, S.-H., Ladner, R., Marks, K., Nelson, S., Pharaoh, A., Trimmer, R., Von
657 Rosenberg, J., Wallace, G., & Weatherall, P. (2009). Global Bathymetry and Elevation
658 Data at 30 Arc Seconds Resolution: SRTM30_PLUS. *Marine Geodesy*, 32(4), 355–371.
659 <https://doi.org/10.1080/01490410903297766>
- 660 Bjørlykke, K., Ramm, M., & Saigal, G. C. (1989). Sandstone diagenesis and porosity
661 modification during basin evolution. *Geologische Rundschau*, 78(1), 243–268.
662 <https://doi.org/10.1007/BF01988363>
- 663 Blakely, R. J. (1988). Curie temperature isotherm analysis and tectonic implications of
664 aeromagnetic data from Nevada. *Journal of Geophysical Research*, 93(B10), 11817–

- 665 11832. <https://doi.org/10.1029/JB093iB10p11817>
- 666 Bonté, D., Van Wees, J. D., & Verweij, J. M. (2012). Subsurface temperature of the onshore
667 Netherlands: New temperature dataset and modelling. *Geologie En*
668 *Mijnbouw/Netherlands Journal of Geosciences*, 91(4), 491–515.
669 <https://doi.org/10.1017/S0016774600000354>
- 670 Boulanouar, A., Rahmouni, A., Boukalouch, M., Samaouali, A., Géraud, Y., Harnafi, M., &
671 Sebbani, J. (2013). Determination of Thermal Conductivity and Porosity of Building Stone
672 from Ultrasonic Velocity Measurements. *Geomaterials*, 03(04), 138–144.
673 <https://doi.org/10.4236/gm.2013.34018>
- 674 Boyer, T. P., Garcia, H. E., Locarnini, R. A., Zweng, M. M., Mishonov, A. V., Reagan, J. R.,
675 Antonov, J. I., Baranova, O. K., Biddle, M. M., Johnson, D. R., & Paver, C. R. (2014). 2013
676 World Ocean Atlas Aids High-Resolution Climate Studies. *Eos, Transactions American*
677 *Geophysical Union*, 95(41), 369–370. <https://doi.org/10.1002/2014EO410002>
- 678 Brigaud, F., Chapman, D. S., & Le Douaran, S. (1990). Estimating thermal conductivity in
679 sedimentary basins using lithologic data and geophysical well logs. *American Association*
680 *of Petroleum Geologists Bulletin*, 74(9), 1459–1477. [https://doi.org/10.1306/0C9B2501-](https://doi.org/10.1306/0C9B2501-1710-11D7-8645000102C1865D)
681 [1710-11D7-8645000102C1865D](https://doi.org/10.1306/0C9B2501-1710-11D7-8645000102C1865D)
- 682 Brigaud, F., Vasseur, G., & Caillet, G. (1992). Thermal state in the north Viking Graben (North
683 Sea) determined from oil exploration well data. *Geophysics*, 57(1), 69–88.
684 <https://doi.org/10.1190/1.1443190>
- 685 Cercone, K. R., & Pollack, H. N. (1991). Thermal maturity of the Michigan Basin. *Special Paper*
686 *of the Geological Society of America*, 256, 1–12. <https://doi.org/10.1130/SPE256-p1>
- 687 CGG. (2019). *Final Report, CGG18M01:Horda/Tampen PSDM, Offshore Norway - North Viking*
688 *Graben (NVG)*.
- 689 Chadwick, A., Arts, R., Eiken, O., Williamson, P., & Williams, G. (2006). Geophysical Monitoring
690 of the CO2 plume at Sleipnir, North Sea. *Nato Science Series: IV: Earth and Environmental*
691 *Sciences*, 65(Advances in the Geological Storage of Carbon Dioxide), 303–314.
692 https://doi.org/10.1007/1-4020-4471-2_25
- 693 Christiansson, P., Faleide, J. I., & Berge, A. M. (2000). Crustal structure in the northern North
694 Sea: An integrated geophysical study. *Geological Society Special Publication*,
695 167(McKenzie 1978), 15–40. <https://doi.org/10.1144/GSL.SP.2000.167.01.02>
- 696 Christofi, N., & Philip, J. C. (1997). European Microbiology Related to the Subsurface Disposal
697 of Nuclear Waste. In P. S. Amy & D. L. Haldeman (Eds.), *Microbiology of the Terrestrial*
698 *Deep Subsurface* (pp. 267–268). CRC Press.
- 699 Copestake, P., Sims, A., Crittenden, S., Hamar, G., Ineson, J., & Bathurst, P. (2003). The
700 Millennium Atlas : Petroleum Geology of the Central and Northern North Sea. In D.
701 Evans, C. Graham, A. Armour, & P. Bathurst (Eds.), *Geological Society of London*.
702 Geological Society of London.
703 <https://doi.org/https://doi.org/10.1017/S0016756803218124>
- 704 Cornelius, C. D. (1975). Geothermal aspects of hydrocarbon exploration in the North Sea Area.
705 *Norges Geologiske Undersøkelse Bulletin*, 316, 29–67.

- 706 Cornford, C. (1998). Source Rocks and Hydrocarbons of the North Sea. In K. W. Glennie (Ed.),
707 *Petroleum Geology of the North Sea* (pp. 376–462). Blackwell Science Ltd.
708 <https://doi.org/10.1002/9781444313413.ch11>
- 709 Cox, D. R., Newton, A. M. W., & Huuse, M. (2020). An introduction to seismic reflection data:
710 acquisition, processing and interpretation. In N. Scarselli, J. Adam, & D. Chiarella (Eds.),
711 *Regional geology and tectonics: principles of geologic analysis* (pp. 571–603). Elsevier.
- 712 Cozier, M. (2019). CCS takes centre stage. *Greenhouse Gases: Science and Technology*, 9(6),
713 1084–1086. <https://doi.org/10.1002/ghg.1942>
- 714 Crameri, F., Shephard, G. E., & Heron, P. J. (2020). The misuse of colour in science
715 communication. *Nature Communications*, 11(1), 5444. [https://doi.org/10.1038/s41467-](https://doi.org/10.1038/s41467-020-19160-7)
716 [020-19160-7](https://doi.org/10.1038/s41467-020-19160-7)
- 717 Dahle, H., Garshol, F., Madsen, M., & Birkeland, N.-K. (2008). Microbial community structure
718 analysis of produced water from a high-temperature North Sea oil-field. *Antonie Van*
719 *Leeuwenhoek*, 93(1–2), 37–49. <https://doi.org/10.1007/s10482-007-9177-z>
- 720 Davies, J. H. (2013). Global map of solid Earth surface heat flow. *Geochemistry, Geophysics,*
721 *Geosystems*, 14(10), 4608–4622. <https://doi.org/10.1002/ggge.20271>
- 722 Davison, I., & Underhill, J. R. (2012). Tectonics and Sedimentation in Extensional Rifts. In D.
723 Gao (Ed.), *Tectonics and Sedimentation* (pp. 15–42). American Association of Petroleum
724 Geologists. <https://doi.org/10.1306/13351547M1001556>
- 725 Duffaut, K., Hokstad, K., Kyrkjeb, R., & Wiik, T. (2018). A simple relationship between thermal
726 conductivity and seismic interval velocity. *Leading Edge*, 37(5), 381–385.
727 <https://doi.org/10.1190/tle37050381.1>
- 728 Eberhart-Phillips, D., Han, D. H., & Zoback, M. D. (1989). Empirical relationships among seismic
729 velocity, effective pressure, porosity, and clay content in sandstone. *Geophysics*, 54(1),
730 82–89. <https://doi.org/10.1190/1.1442580>
- 731 Eiken, O., Ringrose, P., Hermanrud, C., Nazarian, B., Torp, T. A., & Høier, L. (2011). Lessons
732 Learned from 14 years of CCS Operations: Sleipner, In Salah and Snøhvit. *Energy*
733 *Procedia*, 4, 5541–5548. <https://doi.org/10.1016/j.egypro.2011.02.541>
- 734 Esteban, L., Pimienta, L., Sarout, J., Plane, C. D., Haffen, S., Geraud, Y., & Timms, N. E. (2015).
735 Study cases of thermal conductivity prediction from P-wave velocity and porosity.
736 *Geothermics*, 53, 255–269. <https://doi.org/10.1016/j.geothermics.2014.06.003>
- 737 Evans, T. R. (1977). Thermal Properties of North Sea Rocks. *Log Analyst*, 18(2), 3–12.
- 738 Evans, T. R., & Coleman, N. C. (1974). North Sea geothermal gradients. *Nature*, 247(5435), 28–
739 30. <https://doi.org/10.1038/247028a0>
- 740 Færseth, R. B. (1996). Interaction of Permo-Triassic and Jurassic extensional fault-blocks
741 during the development of the northern North Sea. *Journal of the Geological Society*,
742 153(6), 931–944. <https://doi.org/10.1144/gsjgs.153.6.0931>
- 743 Fichler, C., Odinsen, T., Rueslåtten, H., Olesen, O., Vindstad, J. E., & Wienecke, S. (2011).
744 Crustal inhomogeneities in the Northern North Sea from potential field modeling:

- 745 Inherited structure and serpentinites? *Tectonophysics*, 510(1–2), 172–185.
746 <https://doi.org/10.1016/j.tecto.2011.06.026>
- 747 Fossen, H., Pedersen, R. B., Bergh, S., & Andresen, A. (2008). Creation of a mountain chain. In
748 I. B. Ramberg, I. Bryhni, A. Nøttvedt, & K. Rangnes (Eds.), *The Making of a Land: geology*
749 *of Norway* (pp. 178–232). The Norwegian Geological Association.
- 750 Fuchs, S., & Balling, N. (2016). Improving the temperature predictions of subsurface thermal
751 models by using high-quality input data. Part 2: A case study from the Danish-German
752 border region. *Geothermics*, 64, 1–14.
753 <https://doi.org/10.1016/j.geothermics.2016.04.004>
- 754 Fuchs, S., & Förster, A. (2013). Well-log based prediction of thermal conductivity of
755 sedimentary successions: A case study from the north german basin. *Geophysical Journal*
756 *International*, 196(1), 291–311. <https://doi.org/10.1093/gji/ggt382>
- 757 Galson, D. A., Wilson, N. P., Schärli, U., & Rybach, L. (1987). A comparison of the divided-bar
758 and QTM methods of measuring thermal conductivity. *Geothermics*, 16(3), 215–226.
759 [https://doi.org/10.1016/0375-6505\(87\)90001-0](https://doi.org/10.1016/0375-6505(87)90001-0)
- 760 Gautier, D. L. (2005). *Kimmeridgian shales total petroleum system of the North Sea graben*
761 *province*. US Geological Survey.
- 762 Gegenhuber, N., & Schoen, J. (2012). New approaches for the relationship between
763 compressional wave velocity and thermal conductivity. *Journal of Applied Geophysics*,
764 76, 50–55. <https://doi.org/10.1016/j.jappgeo.2011.10.005>
- 765 Goff, J. C. (1983). Hydrocarbon generation and migration from Jurassic source rocks in the E
766 Shetland Basin and Viking Graben of the northern North Sea. *Journal - Geological Society*
767 *London*, 140(3), 445–474. <https://doi.org/10.1144/gsjgs.140.3.0445>
- 768 Gosnold, W., & Panda, B. (2002). *The Global Heat Flow Database of the International Heat*
769 *Flow Commission*. <https://doi.org/http://doi.org/10.17616/R3G305>
- 770 Grad, M., & Tiira, T. (2009). The Moho depth map of the European Plate. *Geophysical Journal*
771 *International*, 176(1), 279–292. <https://doi.org/10.1111/j.1365-246X.2008.03919.x>
- 772 Grevemeyer, I., & Villinger, H. (2001). Gas hydrate stability and the assessment of heat flow
773 through continental margins. *Geophysical Journal International*, 145, 647–660.
774 <https://doi.org/ISI:000169428800007>
- 775 Gu, Y., Rühaak, W., Bär, K., & Sass, I. (2017). Using seismic data to estimate the spatial
776 distribution of rock thermal conductivity at reservoir scale. *Geothermics*, 66, 61–72.
777 <https://doi.org/10.1016/j.geothermics.2016.11.007>
- 778 Haaland, H. J., Furnes, H., & Martinsen, O. J. (2000). Paleogene tuffaceous intervals, Grane
779 Field (Block 25/11), Norwegian North Sea: their depositional, petrographical,
780 geochemical character and regional implications. *Marine and Petroleum Geology*, 17(1),
781 101–118. [https://doi.org/10.1016/S0264-8172\(99\)00009-4](https://doi.org/10.1016/S0264-8172(99)00009-4)
- 782 Harper, M. L. (1971). Approximate geothermal gradients in the North Sea basin. *Nature*,
783 230(5291), 235–236. <https://doi.org/10.1038/230235a0>

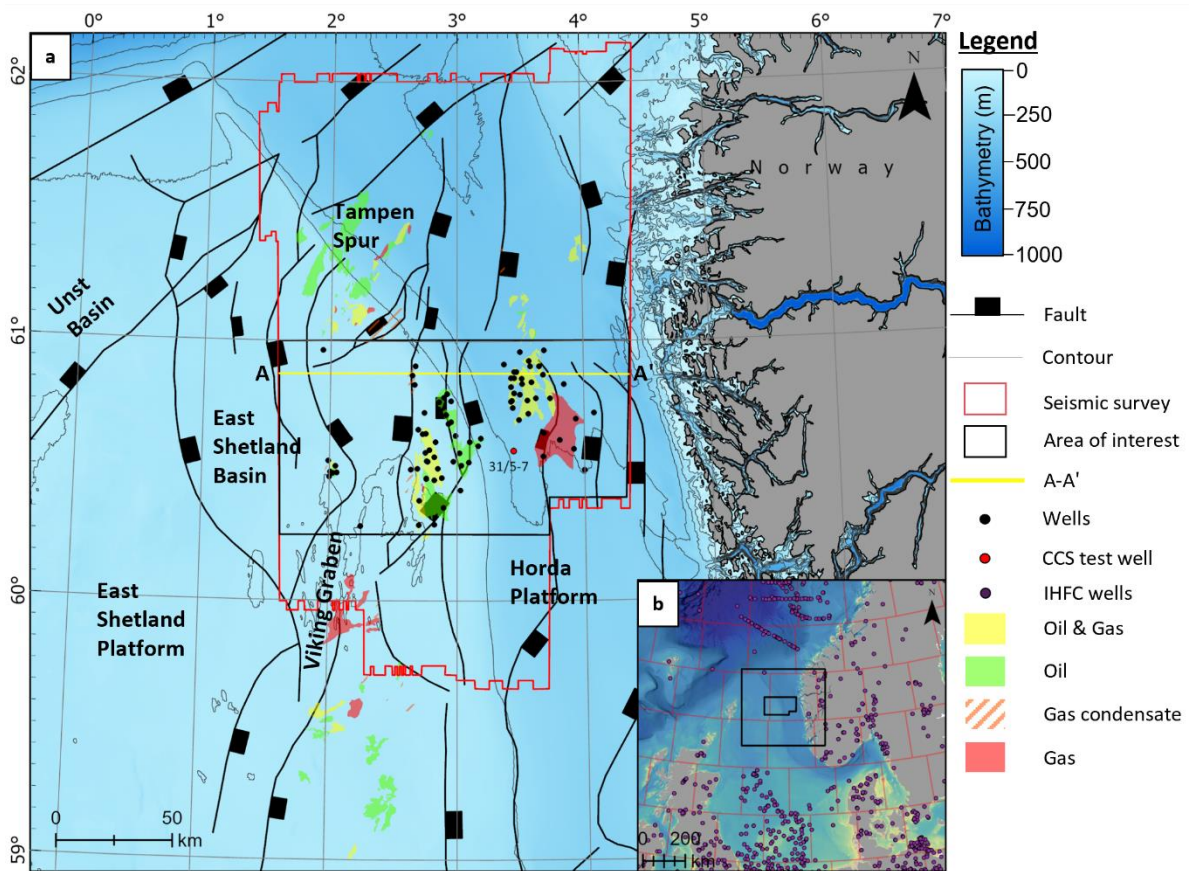
- 784 Hartmann, A. Ā., Rath, V., & Clauser, C. (2005). Thermal conductivity from core and well log
785 data. *International Journal of Rock Mechanics and Mining Sciences*, 42(7-8 SPEC. ISS.),
786 1042–1055. <https://doi.org/10.1016/j.ijrmms.2005.05.015>
- 787 Hasterok, D. (2010). *Thermal State of Continental and Oceanic Lithosphere*. The University of
788 Utah.
- 789 Hasterok, D., Chapman, D. S., & Davis, E. E. (2011). Oceanic heat flow: Implications for global
790 heat loss. *Earth and Planetary Science Letters*, 311(3–4), 386–395.
791 <https://doi.org/10.1016/j.epsl.2011.09.044>
- 792 Hazen, T. C. (1997). Bioremediation. In P. S. Amy & D. L. Haldeman (Eds.), *The Microbiology of*
793 *the Terrestrial Deep Subsurface* (pp. 247–266). CRC Press.
- 794 Hokstad, K., Tašárová, Z. A., Clark, S. A., Kyrkjebø, R., Duffaut, K., Fichler, C., & Wiik, T. (2017).
795 Radiogenic heat production in the crust from inversion of gravity and magnetic data.
796 *Norsk Geologisk Tidsskrift*, 97(3), 241–254. <https://doi.org/10.17850/njg97-3-04>
- 797 Horai, K. (1982). Thermal Conductivity of Sediments and Igneous Rocks Recovered during
798 Deep Sea Drilling Project Leg 60. In D. M. Hussong & S. Uyeda (Eds.), *Initial Reports of the*
799 *Deep Sea Drilling Project*, 60 (Vol. 60, pp. 807–834). U.S. Government Printing Office.
800 <https://doi.org/10.2973/dsdp.proc.60.149.1982>
- 801 Houbolt, J. J. H. C., & Wells, P. R. A. (1980). Estimation of Heat Flow in Oil Wells Based on
802 Relation Between Heat Conductivity and Sound Velocity. *AAPG Bulletin*, 65(7), 1360–
803 1361.
- 804 Jones, I. F. (2018). *Velocities, Imaging, and Waveform Inversion – The evolution of*
805 *characterizing the Earth’s subsurface*. EAGE Publications.
- 806 Jorand, R., Clauser, C., Marquart, G., & Pechinig, R. (2015). Statistically reliable petrophysical
807 properties of potential reservoir rocks for geothermal energy use and their relation to
808 lithostratigraphy and rock composition: The NE Rhenish Massif and the Lower Rhine
809 Embayment (Germany). *Geothermics*, 53, 413–428.
810 <https://doi.org/10.1016/j.geothermics.2014.08.008>
- 811 Justwan, H., Meisingset, I., Dahl, B., & Isaksen, G. H. (2006). Geothermal history and
812 petroleum generation in the Norwegian South Viking Graben revealed by pseudo-3D
813 basin modelling. *Marine and Petroleum Geology*, 23(8), 791–819.
814 <https://doi.org/10.1016/j.marpetgeo.2006.07.001>
- 815 Kubala, M., Bastow, M., Thompson, S., Scotchman, I., & Oygard, K. (2003). Geothermal
816 regime, petroleum generation and migration. In D Evans, C. Graham, A. Armour, & P.
817 Bathurst (Eds.), *The Millenium Atlas: Petroleum Geology of the Central and Northern*
818 *North Sea* (pp. 285–315). The Geological Society of London.
- 819 Landrø, M., Solheim, O. A., Hilde, E., Ekren, B. O., & Strønen, L. K. (1999). The Gullfaks 4D
820 seismic study. *Petroleum Geoscience*, 5(3), 213–226.
821 <https://doi.org/10.1144/petgeo.5.3.213>
- 822 Leadholm, R. H., Ho, T. T. Y., & Sahai, S. K. (1985). Heat flow, geothermal gradients and
823 maturation modelling on the Norwegian continental shelf using computer methods. In
824 *Petroleum Geochemistry in Exploration of the Norwegian Shelf* (pp. 131–143). Springer

- 825 Netherlands. https://doi.org/10.1007/978-94-009-4199-1_9
- 826 Lee, M. W. (2003). Elastic properties of overpressured and unconsolidated sediments. In *U.S.*
827 *Geological Survey Bulletin* (Vol. 2214). <https://pubs.er.usgs.gov/publication/b2214>
- 828 Licciardi, A., England, R. W., Piana Agostinetti, N., & Gallagher, K. (2020). Moho depth of the
829 British Isles: a probabilistic perspective. *Geophysical Journal International*, 221(2), 1384–
830 1401. <https://doi.org/10.1093/gji/ggaa021>
- 831 Lister, C. R. B. (1972). On the Thermal Balance of a Mid-Ocean Ridge. *Geophysical Journal*
832 *International*, 26(5), 515–535. <https://doi.org/10.1111/j.1365-246X.1972.tb05766.x>
- 833 Locarnini, R. A., Mishonov, A. V, Antonov, J. I., Boyer, T. P., Garcia, H. E., Baranova, O. K.,
834 Zweng, M. M., Paver, C. R., Reagan, J. R., Johnson, D. R., Hamilton, M., & Seidov, D.
835 (2013). *WORLD OCEAN ATLAS 2013: Temperature Volume 1* (Vol. 1, Issue NOAA Atlas
836 NESDID 81). <https://doi.org/10.7289/V55X26VD>
- 837 Løseth, H., Øygarden, B., Nygård, A., & Raulline, B. (2016). Reply to Discussion on ‘Late
838 Cenozoic geological evolution of the northern North Sea: development of a Miocene
839 unconformity reshaped by large-scale Pleistocene sand intrusion’, *Journal of the*
840 *Geological Society* , 170, 133–145 [Article]. *Journal of the Geological Society*, 173(2),
841 394–397. <https://doi.org/10.1144/jgs2015-104>
- 842 Løseth, H., Raulline, B., & Nygård, A. (2013). Late Cenozoic geological evolution of the
843 northern North Sea: development of a Miocene unconformity reshaped by large-scale
844 Pleistocene sand intrusion. *Journal of the Geological Society*, 170(1), 133–145.
845 <https://doi.org/10.1144/jgs2011-165>
- 846 Lucazeau, F. (2019). Analysis and Mapping of an Updated Terrestrial Heat Flow Data Set.
847 *Geochemistry, Geophysics, Geosystems*, 20(8), 4001–4024.
848 <https://doi.org/10.1029/2019GC008389>
- 849 Lucazeau, F., & Le Douaran, S. (1985). The blanketing effect of sediments in basins formed by
850 extension: a numerical model. Application to the Gulf of Lion and Viking graben. *Earth*
851 *and Planetary Science Letters*, 74(1), 92–102. [https://doi.org/10.1016/0012-](https://doi.org/10.1016/0012-821X(85)90169-4)
852 [821X\(85\)90169-4](https://doi.org/10.1016/0012-821X(85)90169-4)
- 853 Lucazeau, Francis, Brigaud, F., & Bouroulllec, J. L. (2004). High-resolution heat flow density in
854 the lower Congo basin. *Geochemistry, Geophysics, Geosystems*, 5(3), Q03001.
855 <https://doi.org/10.1029/2003GC000644>
- 856 Mareschal, J., & Jaupart, C. (2013). Radiogenic heat production, thermal regime and evolution
857 of continental crust. *Tectonophysics*, 609, 524–534.
858 <https://doi.org/10.1016/j.tecto.2012.12.001>
- 859 Mavko, G., Mukerji, T., & Dvorkin, J. (2009). *The rock physics handbook : tools for seismic*
860 *analysis of porous media* (T. Mukerji 1965-, J. Dvorkin 1953-, T. Mukerji 1965- author, &
861 J. Dvorkin 1953- author (eds.); 2nd ed.). Cambridge : Cambridge University Press.
- 862 Meert, J. G., & Torsvik, T. H. (2003). The making and unmaking of a supercontinent: Rodinia
863 revisited. *Tectonophysics*, 375(1–4), 261–288. [https://doi.org/10.1016/S0040-](https://doi.org/10.1016/S0040-1951(03)00342-1)
864 [1951\(03\)00342-1](https://doi.org/10.1016/S0040-1951(03)00342-1)

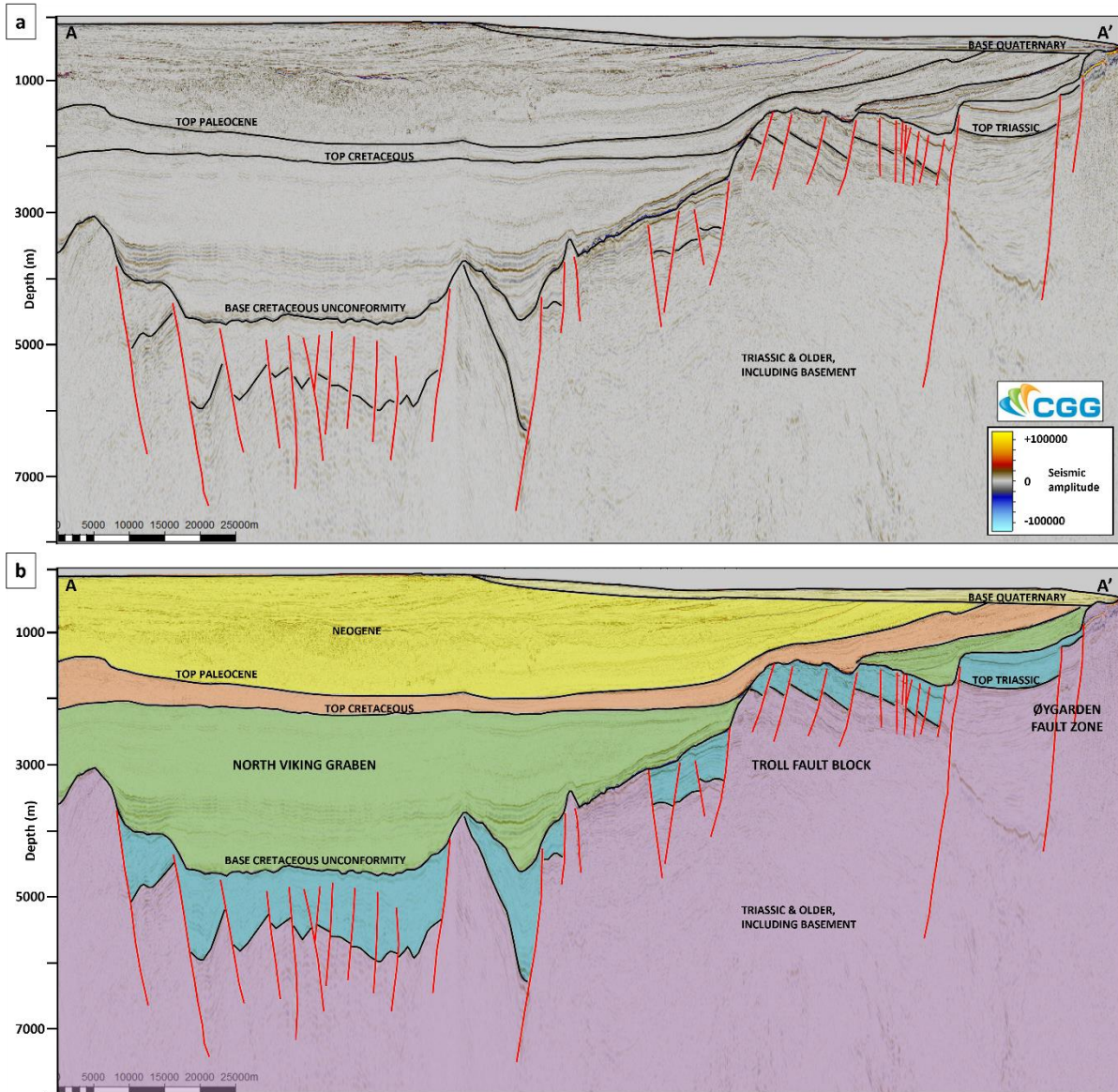
- 865 Mielke, P., Bär, K., & Sass, I. (2017). Determining the relationship of thermal conductivity and
 866 compressional wave velocity of common rock types as a basis for reservoir
 867 characterization. *Journal of Applied Geophysics*, *140*, 135–144.
 868 <https://doi.org/10.1016/j.jappgeo.2017.04.002>
- 869 Nadeau, P. H. (2011). Earth's energy "Golden Zone": a synthesis from mineralogical research.
 870 *Clay Minerals*, *46*(1), 1–24. <https://doi.org/10.1180/claymin.2011.046.1.1>
- 871 Nottvedt, A., Gabrielsen, R. H., & Steel, R. J. (1995). Tectonostratigraphy and sedimentary
 872 architecture of rift basins, with reference to the northern North Sea. *Marine and*
 873 *Petroleum Geology*, *12*(8), 881–901. [https://doi.org/10.1016/0264-8172\(95\)98853-W](https://doi.org/10.1016/0264-8172(95)98853-W)
- 874 Philip, G. M., & Watson, D. F. (1982). A Precise Method for Determining Contoured Surfaces.
 875 *The APPEA Journal*, *22*(1), 205–212. <https://doi.org/doi.org/10.1071/AJ81016>
- 876 Pimienta, L., Klitzsch, N., & Clauser, C. (2018). Comparison of thermal and elastic properties
 877 of sandstones: Experiments and theoretical insights. *Geothermics*, *76*(June), 60–73.
 878 <https://doi.org/10.1016/j.geothermics.2018.06.005>
- 879 Pollack, H. N., Hurter, S. J., & Johnson, J. R. (1993). Heat flow from the Earth's interior: Analysis
 880 of the global data set. *Reviews of Geophysics*, *31*(3), 267.
 881 <https://doi.org/10.1029/93RG01249>
- 882 Popov, Y. A., Pribnow, D. F. C., Sass, J. H., Williams, C. F., & Burkhardt, H. (1999).
 883 Characterization of rock thermal conductivity by high-resolution optical scanning.
 884 *Geothermics*, *28*(2), 253–276. [https://doi.org/10.1016/S0375-6505\(99\)00007-3](https://doi.org/10.1016/S0375-6505(99)00007-3)
- 885 Popov, Y., Tertychnyi, V., Romushkevich, R., Korobkov, D., & Pohl, J. (2003). Interrelations
 886 Between Thermal Conductivity and Other Physical Properties of Rocks: Experimental
 887 Data. *Pure and Applied Geophysics*, *160*(5), 1137–1161.
 888 <https://doi.org/10.1007/PL00012565>
- 889 Posamentier, H. W. (2004). Seismic Geomorphology: Imaging Elements of Depositional
 890 Systems from Shelf to Deep Basin Using 3D Seismic Data: Implications for Exploration
 891 and Development. *Geological Society, London, Memoirs*, *29*(1), 11–24.
 892 <https://doi.org/10.1144/GSL.MEM.2004.029.01.02>
- 893 Prada, M., Lavoué, F., Saqab, M. M., O'Reilly, B. M., Lebedev, S., Walsh, J. J., & Childs, C.
 894 (2019). Across-axis variations in petrophysical properties of the North Porcupine Basin,
 895 offshore Ireland: New insights from long-streamer traveltime tomography. *Basin*
 896 *Research*, *31*(1), 59–76. <https://doi.org/10.1111/bre.12308>
- 897 Pribnow, D. F. C., Kinoshita, M., & Stein, C. . (2000). Thermal data collection and heat flow
 898 recalculations for ODP Legs 101-180. In *Institute for Joint Geoscientific Research*.
 899 <http://www-odp.tamu.edu/publications/heatflow/>
- 900 Purvis, S., Caughtry, N., Mann, J., & Rumyantseva, A. (2018). *Northern Viking Graben Well*
 901 *Study* (Issue 10592).
- 902 Rajaram, M., Anand, S. P., Hemant, K., & Purucker, M. E. (2009). Curie isotherm map of Indian
 903 subcontinent from satellite and aeromagnetic data. *Earth and Planetary Science Letters*,
 904 *281*(3–4), 147–158. <https://doi.org/10.1016/j.epsl.2009.02.013>

- 905 Ritter, U., Zielinski, G. W., Weiss, H. M., Zielinski, R. L. B., & Sættem, J. (2004). Heat flow in the
906 Vøring Basin, Mid-Norwegian Shelf. *Petroleum Geoscience*, 10(4), 353–365.
907 <https://doi.org/10.1144/1354-079303-616>
- 908 Rüpke, L. H., Schmalholz, S. M., Schmid, D. W., & Podladchikov, Y. Y. (2008). Automated
909 thermotectonostratigraphic basin reconstruction: Viking Graben case study. *AAPG*
910 *Bulletin*, 92(3), 309–326. <https://doi.org/10.1306/11140707009>
- 911 Sarkar, A. D. (2020). *Reflection Seismic Thermometry* [University of Manchester].
912 <https://doi.org/10.31237/osf.io/fk7pb>
- 913 Sarkar, A. D., & Huuse, M. (2018). Subsurface Temperature Prediction From Seismic
914 Measurements: A 3-D Seismic Case Study From The Lüderitz Basin, Offshore Namibia.
915 *AAPG International Conference and Exhibition*.
916 <https://www.searchanddiscovery.com/abstracts/html/2018/ice2018/abstracts/296533>
917 7.html
- 918 Sarkar, A. D., & Huuse, M. (2021). Thermal regime of Blake Ridge using seismic and borehole
919 data. *Geochemistry, Geophysics, Geosystems*, (in prep.), 1–41.
920 <https://doi.org/doi.org/10.1002/essoar.10506898.1>
- 921 Schön, J. H. (2015a). Appendix. In *Physical Properties of Rocks* (Vol. 65, Issue 1995, pp. 445–
922 453). <https://doi.org/10.1016/B978-0-08-100404-3.10000-9>
- 923 Schön, J. H. (2015b). Thermal Properties. In *Developments in Petroleum Science* (Vol. 65, pp.
924 369–414). <https://doi.org/10.1016/B978-0-08-100404-3.00009-3>
- 925 The GEBCO_2019 Grid - a continuous terrain model of the global oceans and land. (2019). In
926 *GEBCO Bathymetric Compilation Group*. British Oceanographic Data Centre, National
927 Oceanography Centre, NERC, UK. [https://doi.org/10.5285/836f016a-33be-6ddc-e053-](https://doi.org/10.5285/836f016a-33be-6ddc-e053-6c86abc0788e)
928 6c86abc0788e
- 929 Velde, B. (1996). Compaction trends of clay-rich deep sea sediments. *Marine Geology*, 133(3–
930 4), 193–201. [https://doi.org/10.1016/0025-3227\(96\)00020-5](https://doi.org/10.1016/0025-3227(96)00020-5)
- 931 Wangen, M. (1995). The blanketing effect in sedimentary basins. *Basin Research*, 7(4), 283–
932 298. <https://doi.org/10.1111/j.1365-2117.1995.tb00118.x>
- 933 Warner, M., Ratcliffe, A., Nangoo, T., Morgan, J., Umpleby, A., Shah, N., Vinje, V., Štekl, I.,
934 Guasch, L., Win, C., Conroy, G., & Bertrand, A. (2013). Anisotropic 3D full-waveform
935 inversion. *Geophysics*, 78(2), R59–R80. <https://doi.org/10.1190/geo2012-0338.1>
- 936 Watson, D. F., & Philip, G. M. (1985). A refinement of inverse distance weighted interpolation.
937 *Geoprocessing*, 2(4), 315–327.
- 938 Zamora, M., Vo-Thanh, D., Bienfait, G., & Poirier, J. P. (1993). An empirical relationship
939 between thermal conductivity and elastic wave velocities in sandstone. *Geophysical*
940 *Research Letters*, 20(16), 1679–1682. <https://doi.org/10.1029/92GL02460>
- 941 Ziegler, P. A. (1992). North Sea rift system. *Tectonophysics*, 208(1–3), 55–75.
942 [https://doi.org/10.1016/0040-1951\(92\)90336-5](https://doi.org/10.1016/0040-1951(92)90336-5)
- 943

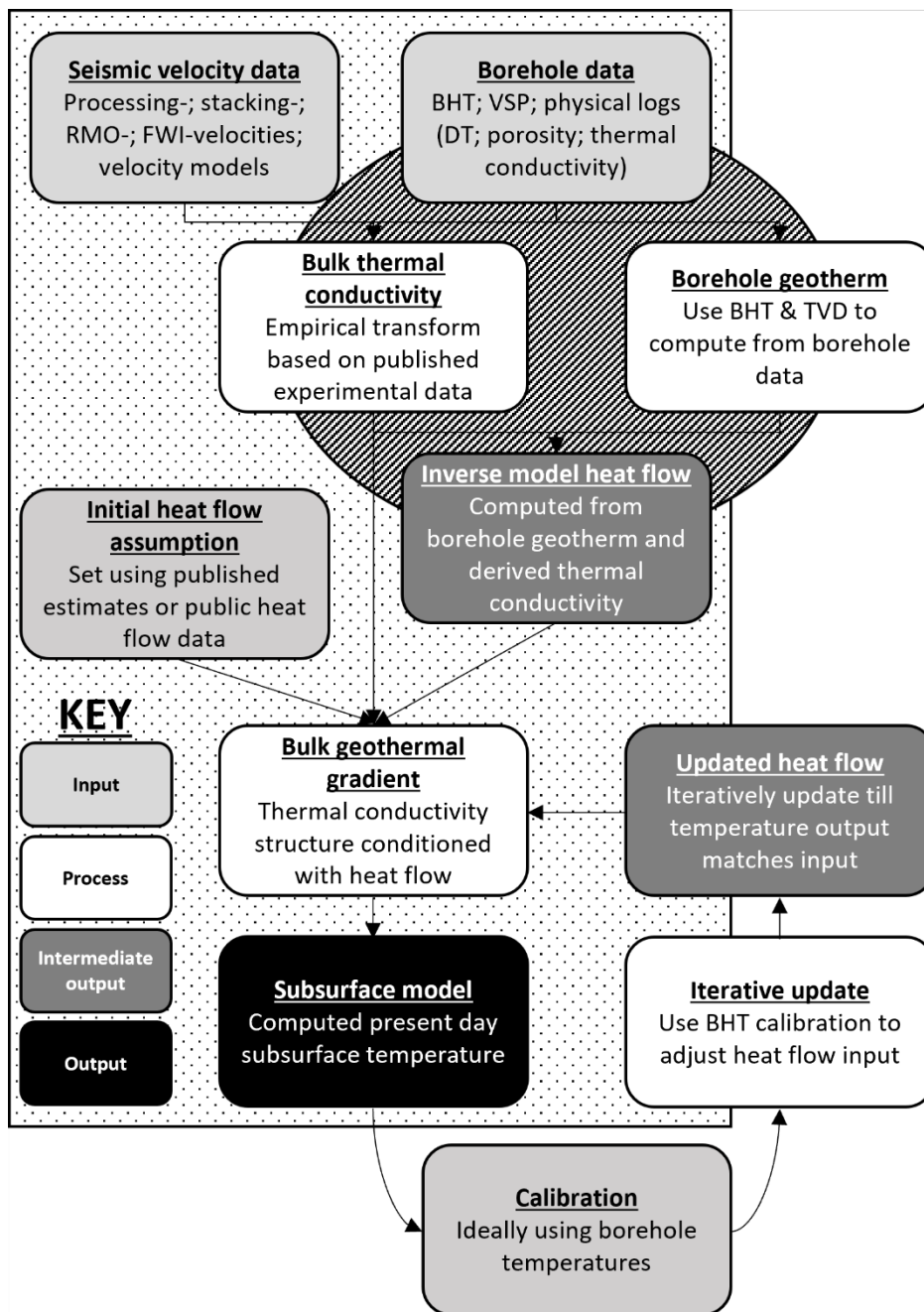
944 9. Figures



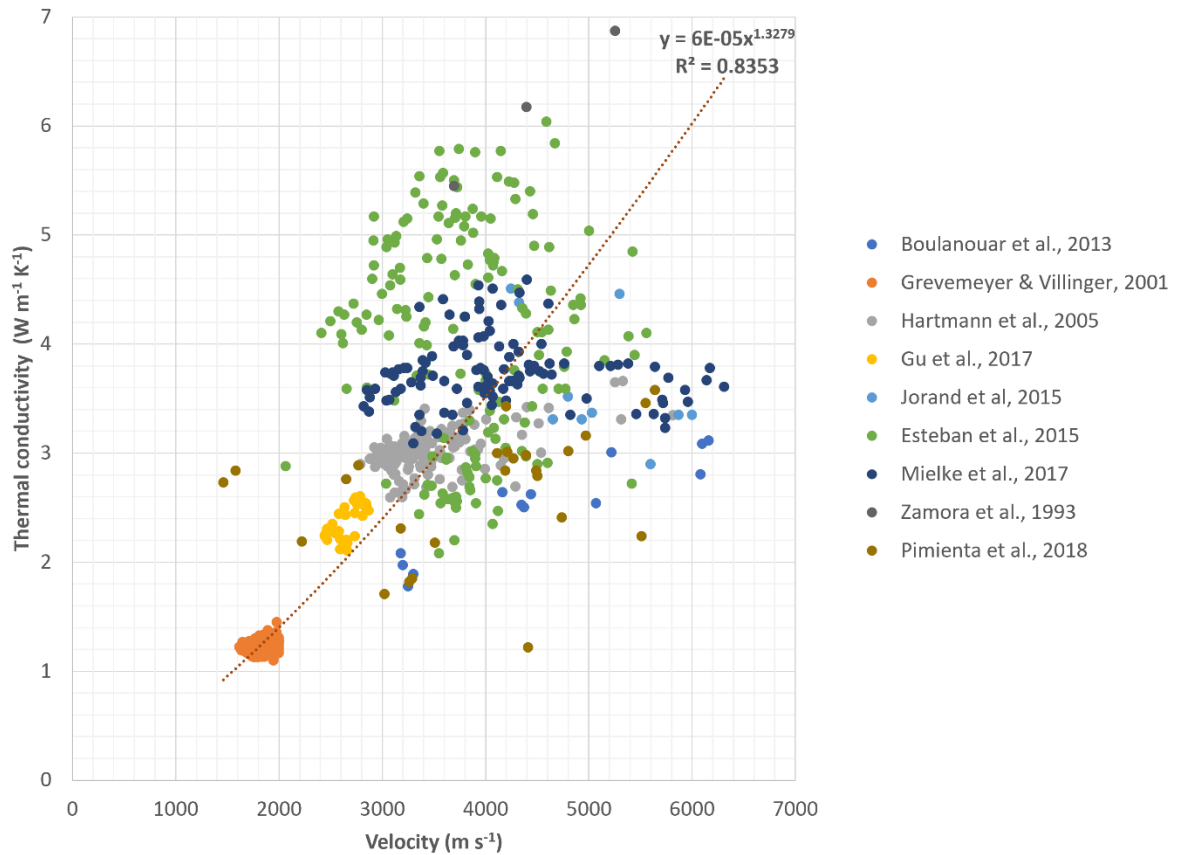
945
 946 *Figure 1: (a) Study area in the northern North Sea outlining the extent of the CGG NVG*
 947 *survey (displayed in red) offshore the Norwegian continental shelf with structural features*
 948 *displayed from (Færseth, 1996). Transect A-A' based on NVG type section (Copestake et al.,*
 949 *2003). Exploration wells displayed are used for calibration. Northern Lights CCS test well*
 950 *31/5-7 also displayed (red circle) (between Brage and Troll fields). Bathymetry from*
 951 *Generalised Bathymetric Chart of the Oceans (GEBCO) (Becker et al., 2009; "The*
 952 *GEBCO_2019 Grid - a continuous terrain model of the global oceans and land," 2019). (b)*
 953 *Existing heatflow data from the IHFC (purple points) shows a scarcity of data in the model*
 954 *area (Gosnold & Panda, 2002). Relying on published heatflow grids such as the Davies (2013)*
 955 *shown above (red grid) demonstrates the coarseness of the data when compared to the*
 956 *scale of the model area (Davies, 2013).*
 957



958
 959 *Figure 2: (a) East West transect A-A' displaying reflection seismic data, annotated with*
 960 *major chronostratigraphic surfaces and structures of note. (b) Overlay of major intervals*
 961 *highlighting the geometry of the NVG in the west of the model area, with tilted fault blocks*
 962 *apparent. The study area is bounded to the west by the East Shetland Basin, with the eastern*
 963 *limits coinciding with the Horda platform. Adapted from (Copestake et al., 2003).*
 964



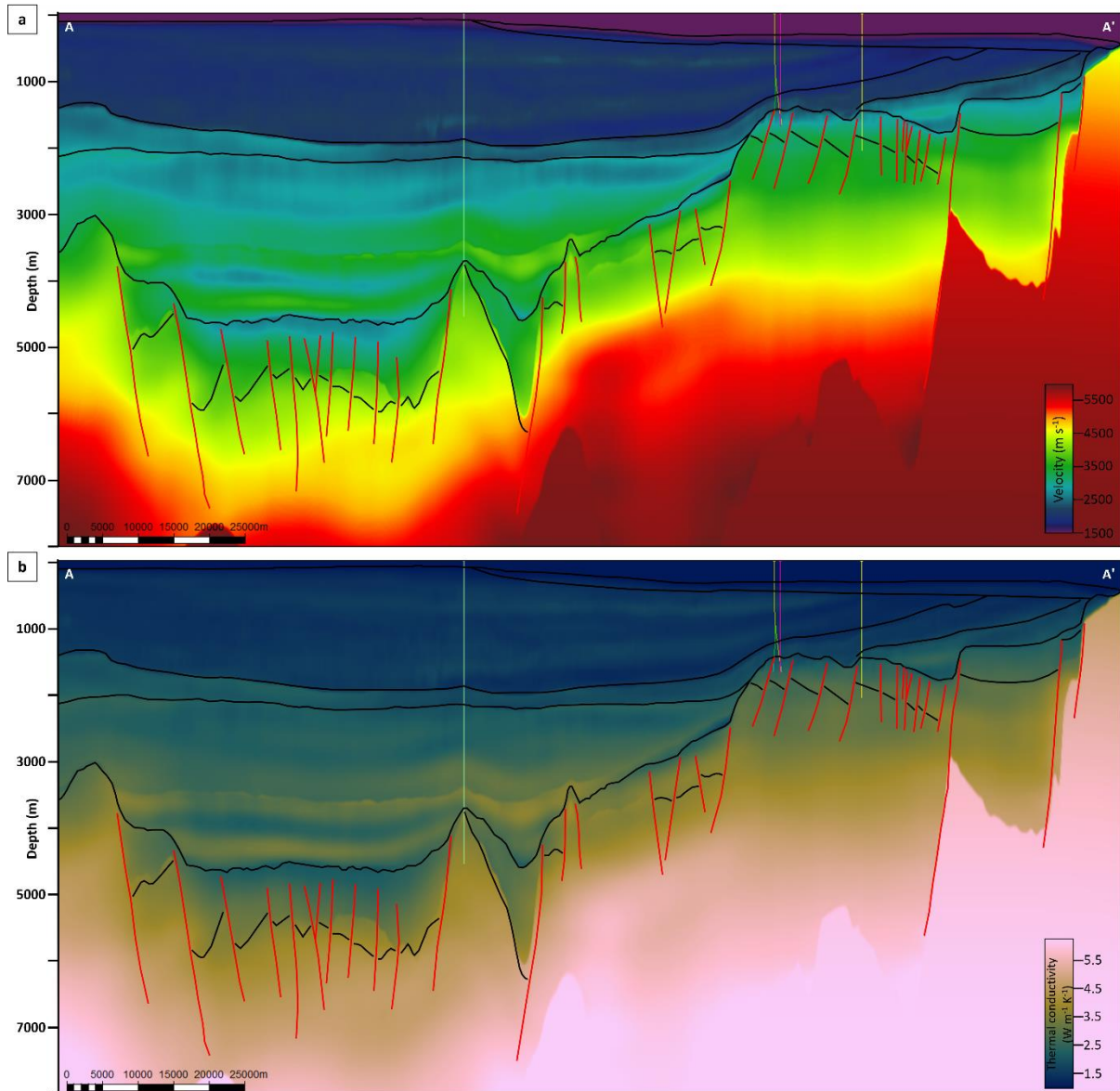
965
 966 *Figure 3: Model building workflow displayed in terms of input, processing steps and*
 967 *outputs/deliverables. There are two main pathways, a forward modelling pathway*
 968 *(demarcated with the dotted background polygon) where seismic data is used to simulate*
 969 *BHTs; and an inverse modelling pathway (demarcated with the hashed background polygon)*
 970 *where BHTs are used to determine the heatflow conditions needed for it. This allows for an*
 971 *iterative final forward modelling pathway utilising the derived heatflow to arrive at a*
 972 *subsurface temperature model representative of present-day conditions.*



974

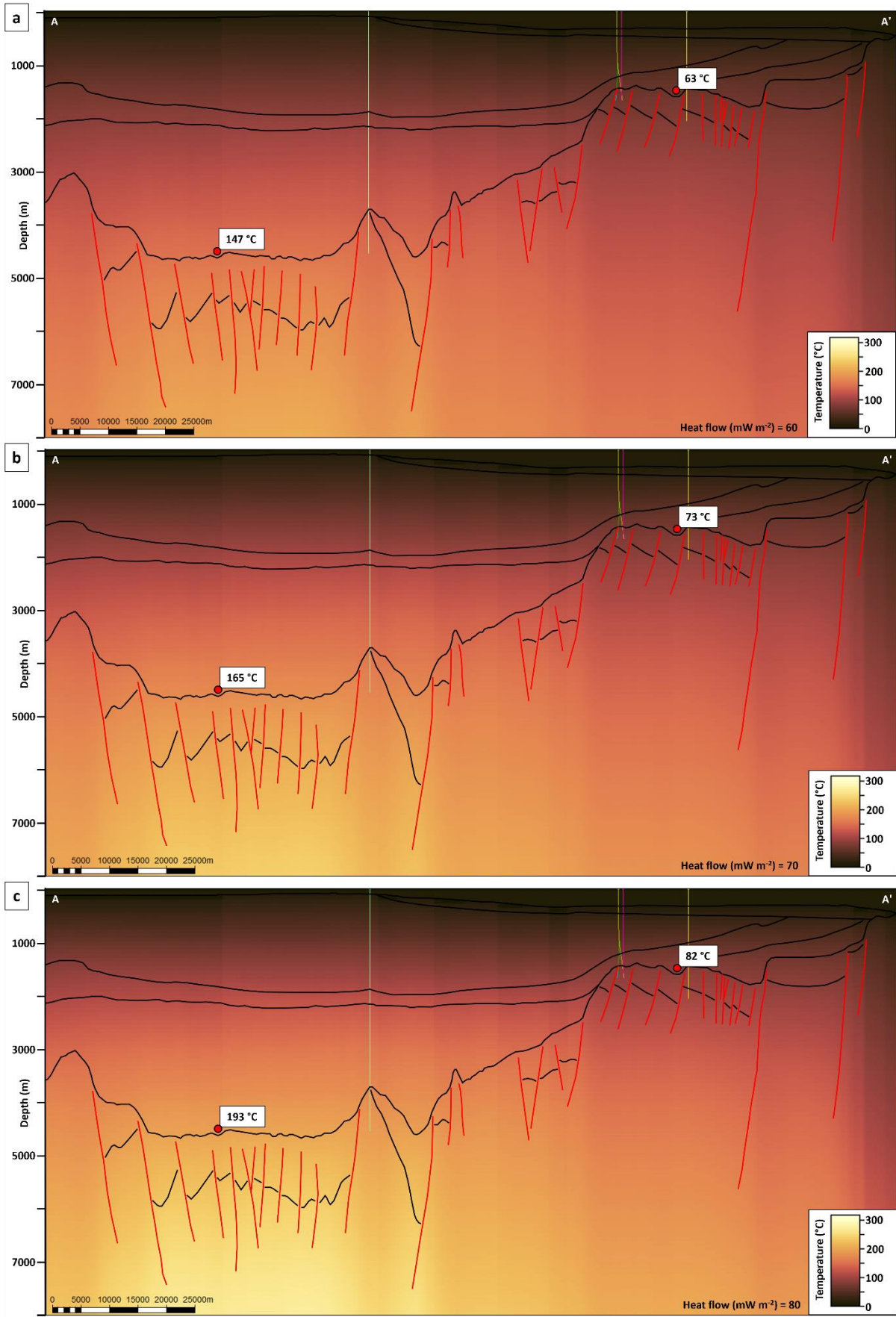
975 *Figure 4: Bulk shift transform from velocity to thermal conductivity derived from*
 976 *experimental data published in the literature. All points displayed are wet samples with*
 977 *laboratory measurements of both velocity and thermal conductivity having been done with*
 978 *similar tools. This is to both reflect the presence of fluids in the subsurface and to also reduce*
 979 *the variables between displayed data respectively.*

980



981
 982
 983
 984

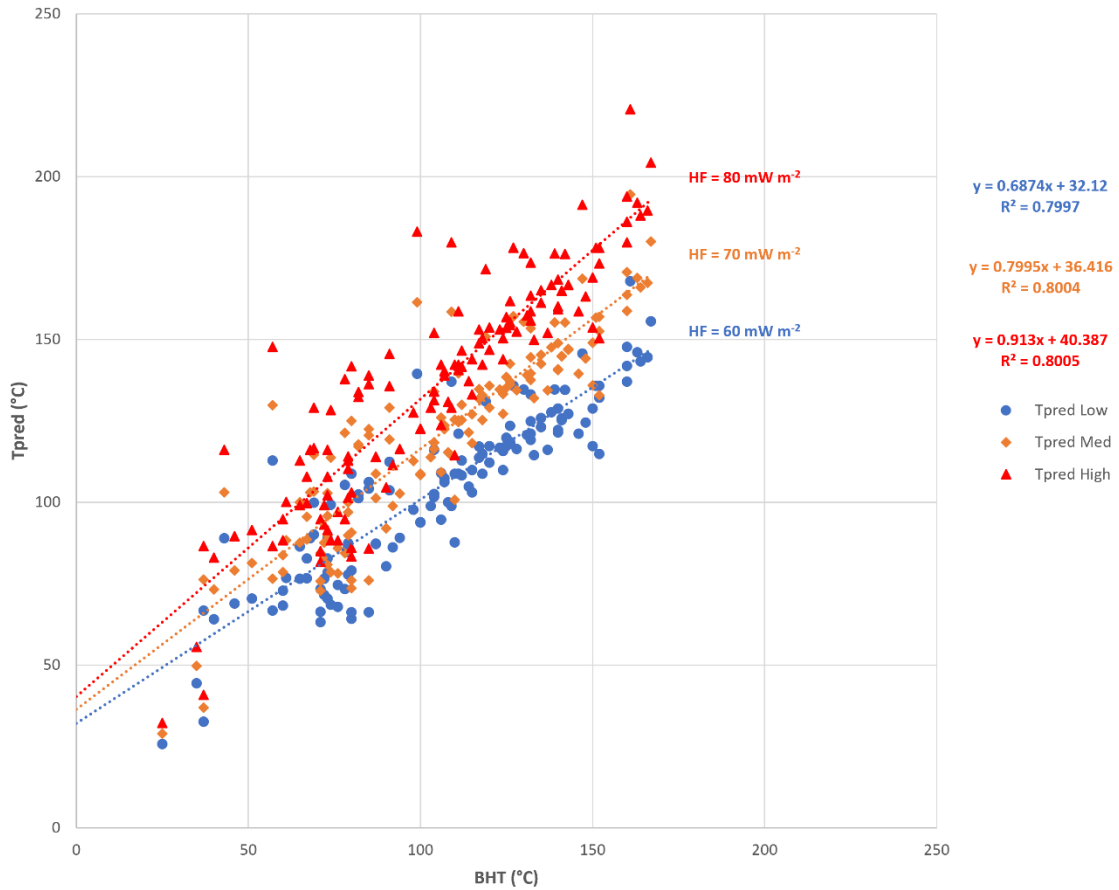
Figure 5: (a) Interval velocities with wells displayed. (b) Instantaneous thermal conductivity from interval velocities using scientific colour bar (Crameri et al., 2020).



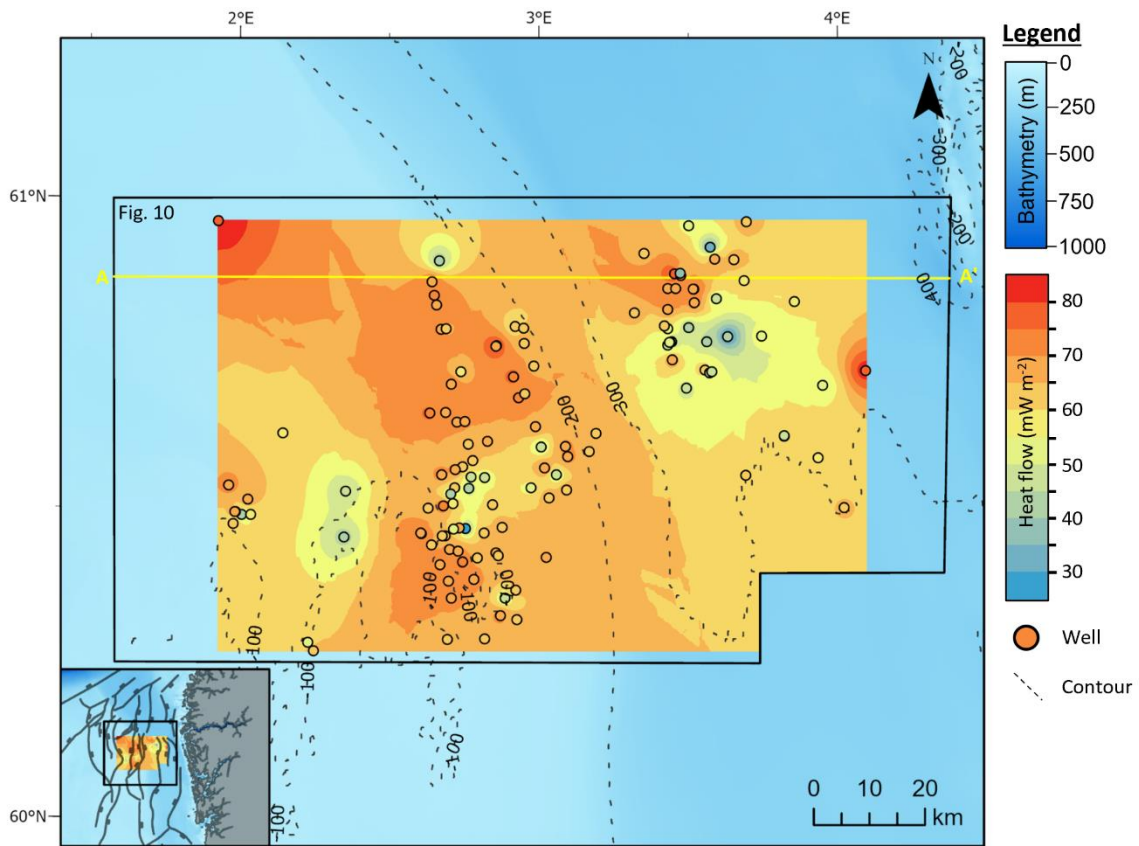
985
986
987

Figure 6: Forward modelling temperature prediction profiles with transect A-A' overlain for (a) low case (60 mW m^{-2}); (b) mid case (70 mW m^{-2}); & (c) high case (80 mW m^{-2}) heatflow

988 scenarios respectively. Temperature readings in the graben centre and on the graben flank
 989 are shown for reference. Highest temperatures are observed in the heart of the graben.
 990 Block like appearance is an artefact of the dimensions of the individual voxels comprising the
 991 thermal model pillar grid used to represent the subsurface.
 992

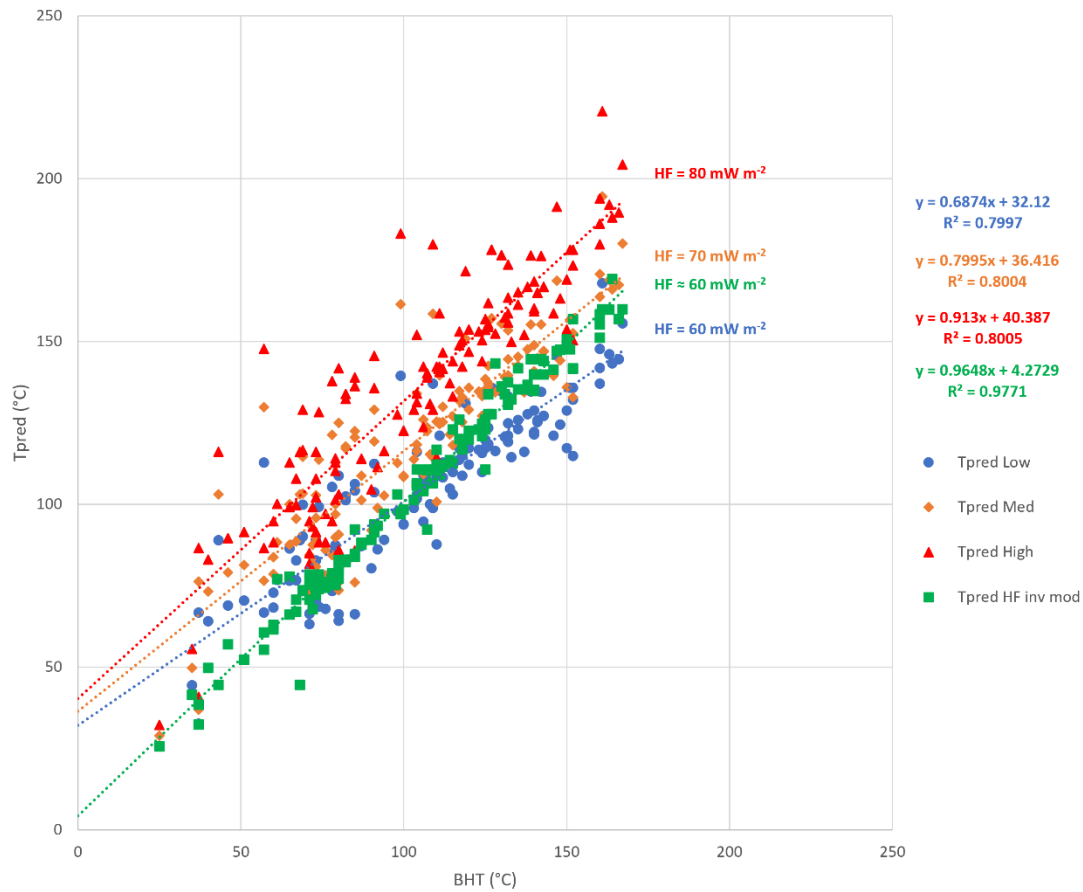


993
 994 *Figure 7: Cross plot of BHT against predicted temperatures (Tpred) for each of the three*
 995 *forward modelling starting conditions for heatflow (low; mid and high case corresponding to*
 996 *60; 70 and 80 mW m⁻² respectively). With increasing input heatflow a corresponding*
 997 *increase is seen in the gradient of the regression line through that set of points.*
 998



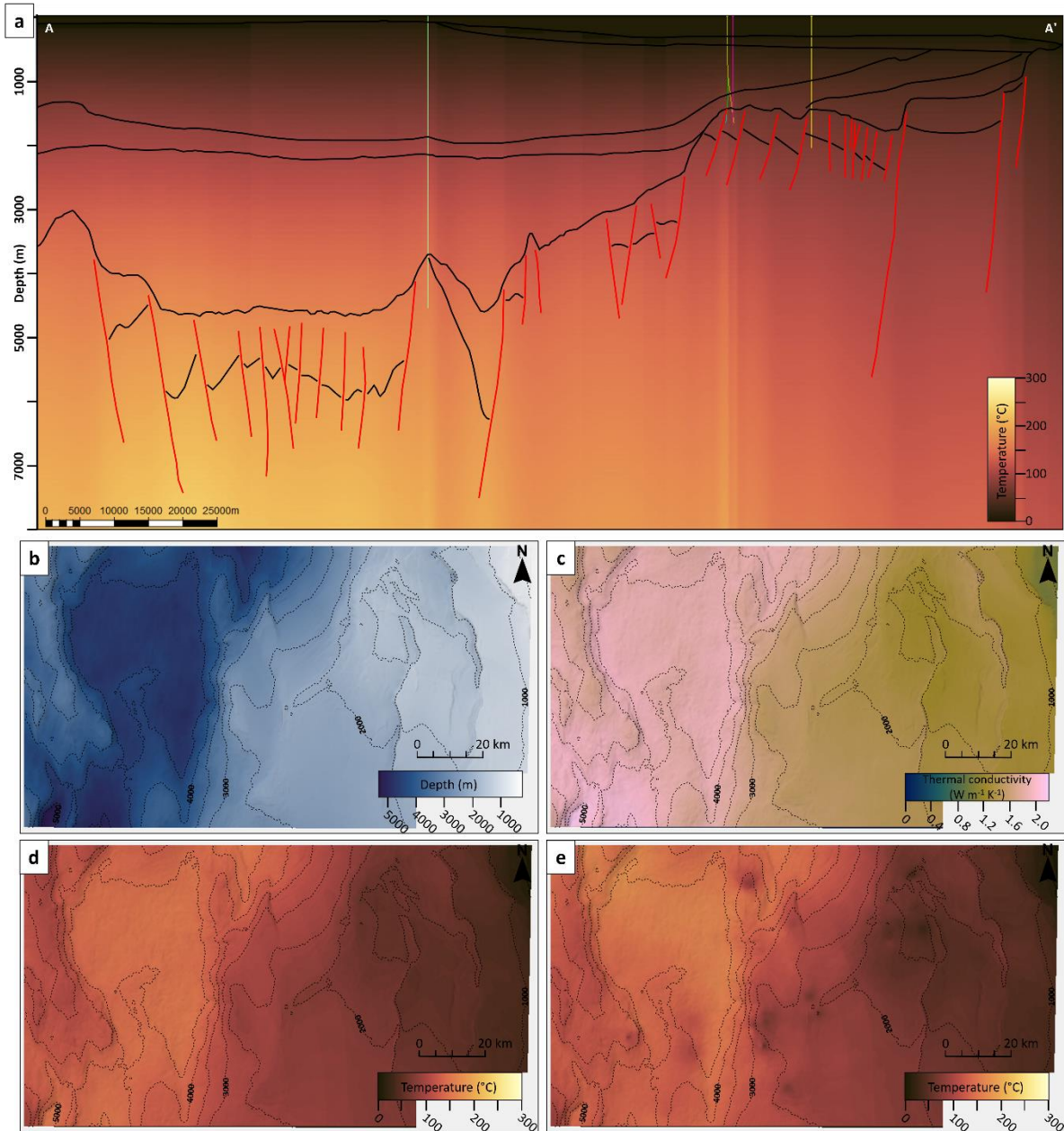
999
 1000
 1001
 1002
 1003

Figure 8: Inverse modelling of heatflow at each well location from BHT and TVD. This data is used to interpolate heatflow across the model area. Interpolated heatflow shows lateral variability at much higher resolution than published global grids.

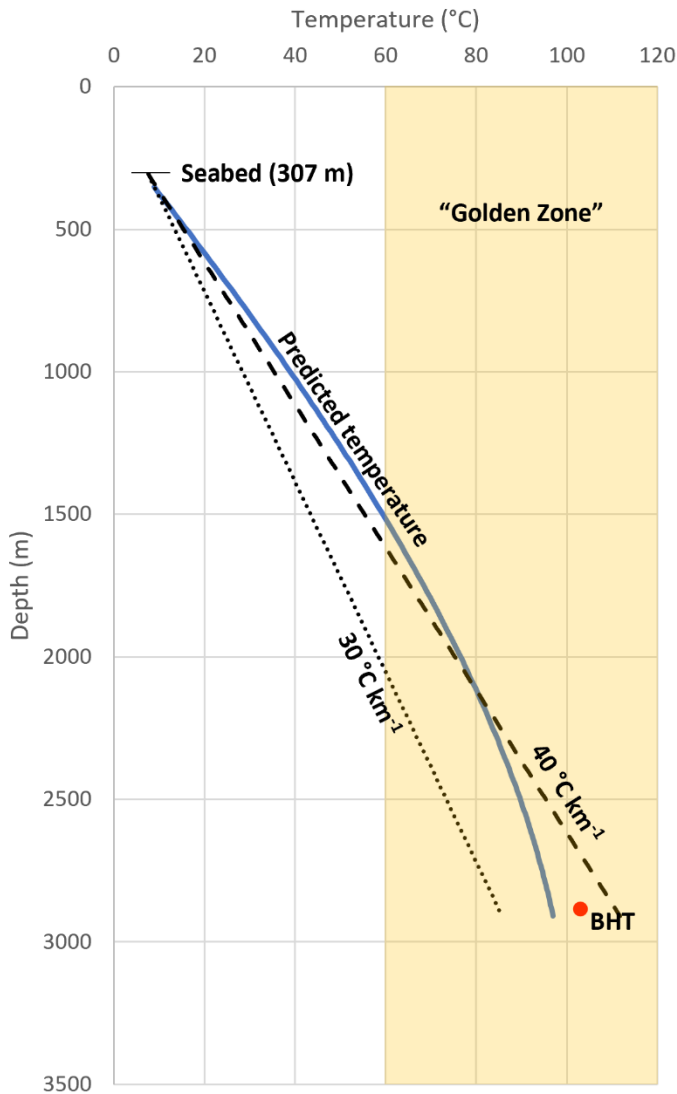


1004
 1005
 1006
 1007
 1008
 1009
 1010

Figure 9: Cross plot of BHT against predicted temperatures (Tpred) with model results using inverse modelling of heatflow across the area displayed (green squares). R-squared for this regression suggests a good statistical fit, the results having a gradient verging on 1:1 as would be expected for results best reflecting the actual subsurface temperature conditions. Furthermore, the spread of points is much narrower for this modelling outcome.



1011
 1012 *Figure 10: (a) Final temperature model produced using inverse modelling of heatflow*
 1013 *overlain on transect A-A' (with well paths and BCU displayed). (b) BCU in depth with 500 m*
 1014 *interval contours shown. (c) RMS amplitude extraction of derived thermal conductivity at*
 1015 *BCU. Where BCU is interpreted to shallow towards the northeast, there are correspondingly*
 1016 *low conductivities that reflect Quaternary sediments in this region instead. (d) Low case*
 1017 *prediction of temperature along BCU. (e) Final temperature prediction using inverse*
 1018 *modelled heatflow along BCU. Comparing with (d) some differences are apparent. Bulls eye*
 1019 *like temperature anomalies in the northeast are likely the translation of the interpolated*
 1020 *heatflow (see Fig. 8).*
 1021



1022
 1023
 1024
 1025
 1026
 1027
 1028
 1029
 1030
 1031
 1032

Figure 11: Modelled subsurface temperature at well 31/5-7 (see Fig. 1) as part of the Northern Lights CCS project. “Golden zone” for sandstone reservoirs is also displayed for context. BHT displayed is from October 2020 data release of preliminary results, indicating that prediction is in close agreement with what was discovered downhole (prediction is offset by 6 °C to reported BHT). Also shown are the temperature profiles taken from seabed assuming a constant linear geothermal gradient. Typically used geothermal gradients in basin modelling are 30 °C km⁻¹ (dotted line) and 40 °C km⁻¹ (dashed line). These are displayed to show how much subsurface temperature predictions may vary using standard processes, particularly at bottom hole (up to ±13 °C).

1033 A.1 Appendix

Source	Geothermal gradient (°C/km)	Heatflow (mW m ⁻²)
(Harper, 1971)	29.7	49.8 – 62.0
(Evans, 1977)		63
(Brigaud et al., 1992)	31.8 – 36.3	50 – 65
(Leadholm et al., 1985)	30 – 35	58.6 – 67
(Justwan et al., 2006)		52.3
(Cornford, 1998)		60 – 82
(Lucazeau & Le Douaran, 1985)		65
(Goff, 1983)	32	57 – 65
(Rüpke et al., 2008)	30 – 40	
(Ritter et al., 2004)		65

1034 *Table A.1: Some examples of reported geothermal gradient and heatflow for the NVG and*
 1035 *surrounding basins from the literature.*

1036

1037